Rethinking Electronic and Geometric Structure of Real Hydrodesulfurization Catalysts by In Situ Photon-In/Photon-Out Spectroscopy

Asma Tougerti*, Pardis Simon, Charlotte Desjacques, Jean Sebastien Girardon, Francesco Mazzanti, Silvio Pipolo, Martine Trentesaux, Sylvain Cristol*

Univ. Lille, CNRS, Centrale Lille, ENSCL, Univ. Artois, UMR 8181 - UCCS - Unité de Catalyse et Chimie du Solide, F-59000 Lille, France

HDS catalysts, Co K edge HERFD XAS, Co RIXS 1s2p, XPS.

ABSTRACT: Core level spectroscopic is a powerful tool to achieve a fine understanding of both the electronic and the geometric structure of heterogeneous catalysts. The present work shows use of Photon-In/Photon-Out Spectroscopy to investigate the structures of hydrodesulfurization catalysts actives sites. Despite countless studies carried out to understand the working phase of this class of catalyst, the exact localization of the promoter (Cobalt) remain an open question for "real HDS catalyst". The difficulty comes from the segregation of cobalt in different phases during the catalyst activation step. As a consequence, most collected spectroscopic signal of cobalt involved in the catalyst, will corresponds to a weighted average of the contributions arising from all cobalt centers (active phase, non-active sulfide phase and the remaining cobalt oxide phase). To overcome this problem, a first time in situ Co K edge

HERFD-XAS is used to discriminate between oxide (Co^{II}-O) and sulfide (Co^{II}-S) phases arising during HDS catalysts activation, allowing the localization of cobalt in the active phase of the catalysts. We find that Co is localized at S-edges of the MoS_2 layers. Furthermore, in situ Co K edge 1s2p RIXS of the sulfided catalyst shows excitations to band-like unoccupied states revealing the metallic nature of cobalt in these structures. A new XPS fitting procedure, considering the exact electronic structure of the active phase is proposed bringing us to reconsider earlier Co-promotion rate published in the literature for a better correlation with the catalytic activity.

INRODUCTION

The paradigm of energy production is shifting from a simple conversion of source material to an emphasis on sustainable energy production based on the development of more efficient and environmental friendly processes in a context of feedstock diversification (heavier feedstock, biomass, …) as well the production of alternative fuels like hydrogen.[1–10] Within this context of chemical industry renewal, heterogeneous catalysts by transition metal sulfides (TMSs) holds great promises as they are used as hydrotreatment catalysts to remove pollutants (S, O, N, and metals) from crude oil[11] and for the treatment of lignocellulosic biomass to reduce their oxygen content (hydrodeoxygenation).[12–14] They also attract a fast-growing interest in the field of hydrogen evolution reaction (HER) and oxygen evolution reaction (OER) to replace the scarce and expensive platinum for electrochemical water splitting which is a fundamental process for the development of fuel cell technology.[4,15]

Due to their economic and environmental relevance TMSs catalysts have been the subject of countless studies by both academic and industrial research centers. It is especially true for hydrodesulfurization (HDS) catalysts [16–22] whose design has been improved continuously to comply with more and more stringent environmental specifications on maximum sulfur content allowed in transportation fuels.[11,23] There is a general consensus that HDS process is now mature for conventional oil, however, there is still a need

1   for improvement in the hydroprocessing of non-standard feedstock that are being more and more im-

2   portant in volume in a context of global decrease of available resources.[11,23] To process these feedstocks,

3   there is a need of cracking large molecule as well desulfurizing them.[22,24]

4   The HDS catalysts are consisting of Co(Ni) promoted nanometer scale Mo(W)S$_2$ particles dispersed on

5   high surface area alumina support (γ-alumina). Combination of Mo with Co (Ni) gives rise to a synergetic

6   effect in HDS activity due to the formation of the so-called active CoMoS phase. Numerous achievements

7   have been obtained during the last twenty years regarding the characterization of the structure of CoMoS

8   phase, thanks mainly to the progress in DFT simulations and to the application of Scanning Tunneling

9   Microscopy (STM) to characterize model HDS catalysts. DFT calculations and STM images of model

10   HDS catalysts (CoMo/Au (111)), revealed that the localization of the promotor occurs at the MoS$_2$ layers

11   edges.[25–27] Non-promoted MoS$_2$ slabs show a triangular morphology[28] that becomes hexagonal in case of

12   promotion by cobalt. [25,26] As for unpromoted MoS$_2$, there are two types of edges for the promoted MoS$_2$:

13   Sulfur-edge (S-edge), which correspond to the edges located along ($\bar{1}010$) MoS$_2$ direction and metal-edge

14   (M-edge) located along the ($10\bar{1}0$) MoS$_2$ direction. STM study show that cobalt atoms are located on the

15   S-edges, while the M-edges remain unpromoted.[25,26] DFT-based Wulff equilibrium morphology calcula-

16   tions showed that under industrial sulfidation conditions (for 100% coverage of Co), the energy of the

17   Co-S-edge is about 0.20 eV (per cobalt atom) more stable than the Co-M-edges which in agreement with

18   STM results showing a 100 % Co-promotion at S-edges.[16] Furthermore, it was reported that the substitu-

19   tion of Mo by Co atoms induces major change in the electronic structure of the S-edges giving rise to

20   "III$_{co}$" edges states which are metallic. Very recent studies shown that such new states play a key role for

21   the desulfurizing of large organosulfur molecules that require hydrogenation of one aromatic ring of the

22   molecule. Indeed, this hydrogenation pathway is initiated by the adsorption of the molecule that is driven

23   by interaction of this conducting state with the π-system of the aromatic ring. Such interaction was not

24   observed for the unpromoted Mo-edges.[29]. However, this metallic character of the Co-S-edges as well as

1   the exact localization of the promotor were only observed for catalysts prepared by surface science tech-

2   niques where dispersed MoS_2 nanoclusters were obtained by the evaporation of the Mo under H_2S atmos-

3   phere on the (111) Au reconstructed surface. This contrasts with usual heterogonous catalysts synthesis

4   that occur in aqueous medium and involve oxide support with high surface area and high porosity. Very

5   recently, the use of α-Al_2O_3 single crystal as substitutes for γ-alumina support, to investigate the specific

6   role of individual support facets of the γ-Al_2O_3 have shown the crucial role of the oxide support on the

7   structure/size/orientation of the MoS_2 active phase.[20] However, such approach has been up to now re-

8   stricted to the non-promoted catalysts (MoS_2 phase) and fails to take into account the influence of the

9   porosity and surface defects presented by γ-Al_2O_3 oxide support.

10   The characterization of the CoMoS phase is still lacking for "real HDS catalysts" due to the segregation

11   of the Co element in different phases during the catalyst preparation and activation steps. As a conse-

12   quence, most collected spectroscopic signal of cobalt involved in the catalyst, will corresponds to a

13   weighted average of the contributions arising from all cobalt centers: the CoMoS active phase, the non-

14   active sulfide phase (Co_xS_y) and the remaining cobalt oxide phase. To overcome this problem and to study

15   the genesis of HDS catalysts, we propose during this work to use site selective $K\beta_{1,3}$ High Energy Reso-

16   lution Fluorescence Detected X-ray Absorption Spectroscopy (HERFD-XAS).[30–32] Indeed, thanks to the

17   advent of new crystal analyzers with high spatial angular acceptance and high-energy resolution it is now

18   possible to select a specific fluorescence channel, allowing a much better separation between the emission

19   lines before photon counting.[33,34] This results in the development of two complementary photon-in pho-

20   ton-out spectroscopies: HERFD-XAS and Resonant Inelastic X-ray Scattering (RIXS).[35] For 3d transition

21   metal, the origin of the $K\beta_{1,3}$ fluorescence line selectivity is the overlap of the 3d valence orbitals with 3p

22   electronic states resulting in a 3p-3d exchange interaction.[36] This induces a shift in the energy of the $K\beta_{1,}$

23   $_3$ line as function of the electronic state of the absorber.[36,37] By aligning the detector to the energy of the

24   $K\beta_{1,3}$ emission line, it is possible to obtain a pure or quasi-pure XAS spectrum of only one absorber atom

25   speciation. Furthermore, partial fluorescence detection mode gives rise to highly resolved XAS spectra as

1 the recorded spectrum is not broadened by the short 1s core hole lifetime but by the longer 2p final state

2 lifetime.[35] On the other hand, RIXS consists in recording emission lines through a resonance (K-edge for

3 1s2p RIXS) that results in a 2D spectrum: the RIXS plane is showing intensity *vs* excitation energy (x-

4 axis) and emission energy (y-axis). [38,33] This allows solving the different contributions of the XAS pre-

5 edge structure by probing the different electronic intermediate states whereas in classical XAS K edge of

6 3d transition metal, the pre-edge corresponds to the sum of these states.[33]

7 Hence, the present work address both electronic and geometric structure of cobalt in "real HDS catalysts"

8 by using two complementary photon-in photon-out spectroscopies. *In situ* Co K edge HERFD-XAS is

9 used for the first time to discriminate between oxide (Co^{II}-O) and sulfide (Co^{II}-S) phases arising during

10 HDS catalysts activation in order to determine the exact localization of the promotor. To investigate

11 whether Co metallic states arise for real catalyst, as suggested by STM images for model HDS catalysts,

12 *in situ* Co K edge 1s2p RIXS is applied to probe the electronic structure of the promotor. The results are

13 then compared to the ones obtained by X-ray Absorption (XAS) and X-ray Photoelectron Spectroscopy

14 (XPS) that are widely used in HDS scientific community for the characterization of HDS catalysts. As a

15 matter of fact, XPS spectra show usually a sulfidation rate of the cobalt between 40 and 60% while XAS

16 suggests an almost total sulfidation of the cobalt oxide phase.[39–47] This disagreement although well known

17 by the HDS scientific community has not been deeply investigated. In the conclusion of this work we will

18 try to tackle this problem and to figure out the origin of this discrepancy.

19

20 EXPERIMENTAL SECTION

21 **Preparation of the catalyst**. Alumina supported Mo promoted by Co catalyst ($CoMo\_Al_2O_3$) was pre-

22 pared by simultaneous incipient wetness impregnation of a solution of Ammonium Heptamolybdate

23 ((NH_4)$Mo_7O_{24} \cdot 4H_2O$) and Co^{III} ethylene diamine ($Co(en)_3 \cdot 6H_2O$) on γ-alumina support with specific sur-

24 face area of 200 m^2/g. The catalyst composition is 11 %wt of Mo with Co/Mo molar ratio of 0.4. It was

25 then calcined 4h at 400 °C in air. Raman spectrum of $CoMo\_Al_2O_3$ show a main line at 967 cm^{-1} and a

1   broad shoulder at about 844 cm^{-1} which are spectral signature characteristic of a polymolybadte species.[48]

2   No further peak line of $CoMoO_4$ oxide (line at 820 cm^{-1}, doublet at 945 and 952 cm^{-1}) or oxide MoO_3

3   (fine lines at 819 and 995 cm^{-1}) are observed on the spectrum (Supporting Information (figure S1)).

4   **In situ photon-in/photon-out spectroscopy.** Co K edge HERFD-XAS and 1s2p RIXS spectra were rec-

5   orded at SOLEIL synchrotron facility (Gif sur Yvette, France) on the GALAXIES beamline.[49] The energy

6   of the incident radiation was selected using fixed-exit Si(111) double-crystal monochromator. Co K edge

7   HERFD-XAS and Co 1s2p RIXS spectra were recorded with spherically bent crystals in a Rowland ge-

8   ometry: the K_α fluorescence line of cobalt was selected by a silicon crystal Si (531) whereas for the K_β

9   fluorescence line of cobalt, a germanium crystal Ge (444) was used. A bag filled with helium was posi-

10   tioned between the sample and the analyzer crystal to limit the absorption of the fluorescence signal into

11   the air. The fluorescence signal was then collected on the avalanche photodiode detector (APD). A pho-

12   tography of this experimental set up is given in Supporting Information (figure S2). The catalyst compo-

13   sition is 4.4 %wt of Co, which rule out any self-absorption effects. The sample placed on the *in situ*

14   catalytic cell[50] was heated up to 400 °C with a ramp of 1 °C/min under a flux of H_2/H_2S (10% H_2S). Note

15   that the acquisition time of one RIXS plane needs 4h making only possible the recording of RIXS planes

16   of the start (room temperature, under air) and the end (400 °C, under a flux of H_2/H_2S) points. Neverthe-

17   less, recording one Co K edge HERFD-XANES spectra needs 3 min making possible to record spectra

18   all along the temperature ramp.

19   **The X-ray photoelectron spectroscopy (XPS).** XPS experiments were carried out in a Kratos AXIS

20   Ultra DLD spectrometer equipped with a hemi-spherical analyser operating at a fixed pass energy of 20

21   eV. The pressure during analysis was lower than 5. 10^{-9} mbar. Before analyses, the samples were freshly

22   sulfided and transferred into the analysis chamber under nitrogen atmosphere to avoid their partial reoxi-

23   dation. The absence of a contribution around 168.9 eV in the S 2p spectrum (which would correspond to

24   sulfates species) is used to check that oxidation of the samples did not occur during the transfer. Powdered

25   samples were deposited on conductive tape and during all the acquisition the Kratos charge compensation

1   system was used. Prior to and after Co 2p energy region analysis, O1s spectra were recorded and compared

2   to make sure that no charge shifting was affecting the spectra. The binding energies and shapes of all

3   spectra from the catalyst present no shifting nor broadening or asymmetrical features as compared to

4   $CoAl_2O_4$ and Co_9S_8 references. Thus, no differential charging effect was ongoing during the XPS analysis

5   that could affect the spectra. All the data was acquired using monochromatic Al Kα radiation (1486.6 eV)

6   operating at 225 W. The binding energies (BE) were corrected taking C 1s (284.8 eV) as reference. The

7   Mo 3d, S 2p, Al 2p, O 1s, Co 2p and Valence Band (VB) spectra were analyzed using the CasaXPS

8   software (version 2.3.16, Casa Software Ltd.).[51] For the Co 2p signal, in order to keep a good energy

9   resolution and to allow decomposition, a 20 eV pass energy was selected for analysis. Thus, to increase

10 the signal to noise ratio, 70 scans were acquired on the Co 2p energy range with a step of 50 meV and an

11 acquisition dwell time of 300 ms, leading to a total acquisition time for the Co 2p spectra only of 6.4 h.

12 Spectra decomposition and quantification was performed after a Shirley type background subtraction and

13 Gaussian–Lorentzian decomposition parameters with 30/70 Gaussian/Lorentzian proportion, except for

14 metallic Co 2p peak which was fitted with an asymmetric main peak and two plasmon loss peaks at 3.0

15 eV and 5.0 eV above the main peak.[52,53] To remove possible surface oxidation, Co_9S_8 reference compound

16 was pressed as a pellet and analysed after a Cs+ sputtering (1 kV, 65 nA) carried out using a ToF-SIMS

17 V instrument (ION-TOF GmbH Germany) over an area of 500 μm × 500 μm. The reference sample was

18 then transferred under ultra-high vacuum (< 5.10^{-9} mbar) into the XPS analysis chamber. The surface area

19 analyzed on the sample was 110 μm × 110 μm centered on sputter gun crater.

20

21 THEORITICAL SECTION

22 **XANES.** XANES spectra simulations have been performed using the FDMNES package.[54] The FDMNES

23 code is based on real space mono-electronic approach to calculate the XANES spectra of clusters built

24 around each non-equivalent absorbing atom of the structure. To calculate the final states, we used the full

1 potential Finite Difference Method (FDM). The core-hole lifetime (1.3 eV at Co K-edge) was taken into

2 account by applying a convolution procedure to the calculated spectra.[55]

3 **DFT calculations**. Total energy calculations were performed within the Density Functional Theory (DFT)

4 framework using the generalized gradient approximation of Perdew, Burke and Ernzerhof (PBE).[56] The

5 Vienna Ab initio Simulation Package (VASP) was used to solve the Kohn-Sham equations.[57–59] The plane

6 wave basis set to express the electron wave functions was controlled with an energy cut-off of 400 eV.

7 The electron–ion interactions were described within the Projector Augmented Waves (PAW) approach

8 with the pseudopotential files provided with the VASP software.[60,61] The slab, representing the CoMoS

9 structures, is constituted of 4 stoichiometric layers in the z direction (out of which 2 are allowed to relax

10 and two are fixed to simulate the bulk) and the unit cell dimension perpendicular to the surface plane has

11 been chosen large enough to avoid interaction between slabs (*i.e.* a distance of 15 Å is always kept be-

12 tween successive slabs). Two MoS_2 layers are used in the y direction to have both S and M termination

13 for the surface and 4 MoS_2 units are used in the x direction. All calculations are performed with two k-

14 points in the x direction, which, owing to the size of the system under investigation, proved to be sufficient

15 to integrate the Brillouin zone. The geometry of the CoMoS structures were optimized until the modulus

16 of the forces acting on the every atoms was lower than 0.03 eV.$Å^{-1}$ and the total energy variation between

17 successive geometries was below 1 meV.

18

19 RESULTS AND DICUSSION

20 **Electronic structure of cobalt centers in HDS catalysts.** Figure 1 shows overview of the cobalt 1s2p

21 RIXS contour plot of the catalyst recorded under air at room temperature (denoted hereafter as

22 CoMo_Al_2O_3_RT) and at 400 °C under a flux of H_2/H_2S (denoted hereafter as CoMo_Al_2O_3_ H_2S_ 400°C)

23 together with a zoom on the structures around 7709 eV incident energy and 779 eV energy transfer. The

24 incident photon energy range of the Co^{II} 1s2p RIXS planes correspond to the energy range of pre-edge

25 peak of the Co^{II} K edge XANES spectra. Co^{II} 1s2p RIXS occurs through a quadrupole transition from

1    $1s^2 2p^6 3d^7$ ground state to $1s^1 2p^6 3d^8$ intermediate states followed by the $1s^1 2p^6 3d^8$ to $1s^2 2p^5 3d^8$ dipole

2   decay. [33,35,38] The pre-edge structure in the RIXS planes (Figure.1 a) exhibits therefore two resonances

3   due to the splitting of the final states into $2p_{3/2}$ and $2p_{1/2}$ by 2p spin–orbit coupling. Above the energy

4   range of the pre-edge (7712 eV Figure 1.a, b), the observed structures correspond to X-Ray Emission

5   lines $K_{\alpha 1}$ and $K_{\alpha 2}$.[62] The electronic structure of the catalyst undergo a major change after sulfidation as

6   shown by the evolution of RIXS structures form vertical contour for the oxide catalyst (Figure 1.a,c) to

7   a diagonal contour for the sulfide catalyst (Figure 1.b,d).

8
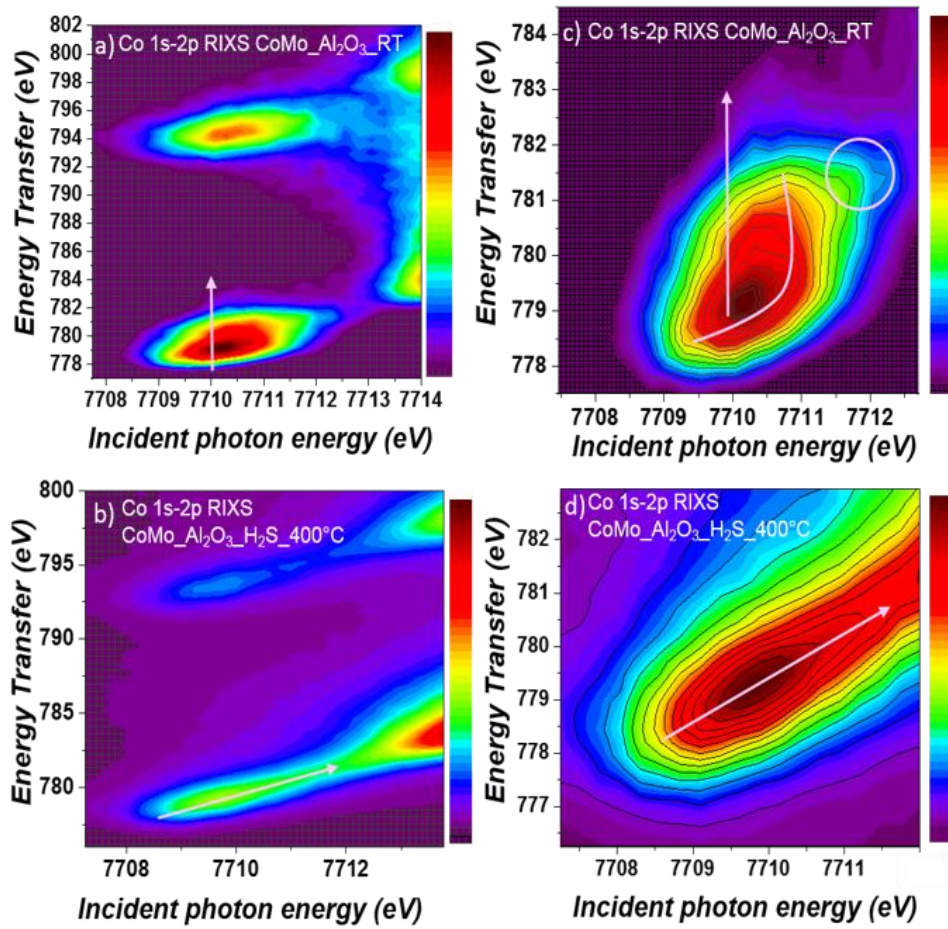
9

10   **Figure 1.** Experimental Co 1s2p RIXS planes of CoMo_Al_2O_3_RT (a) and CoMo_Al_2O_3_H_2S_400°C

11   (b) catalysts. Zoom on the $2p_{3/2}$ resonance on RIXS plane of CoMo_Al_2O_3_RT (c) and

12   CoMo_Al_2O_3_H_2S_400°C (d)

1

2 Figure 2 is a schematic sketch of the RIXS transitions together with a schematic representation of the

3 expected RIXS planes as reported by Glatzel and collaborators in their tremendous effort to provide an

4 accessible way to understand the RIXS process to the scientific community.[33,35] We focus first on the

5 upper part of Figure 2 (A, B) representing RIXS transitions to discrete excited states. Green lines in Figure

6 2.A show that lower energy intermediates states reached by RIXS transitions are detected in the RIXS

7 map at lower incident energy (green circles, Figure 2.B) while states at higher energies (red lines, Figure

8 2.A) are localized at higher incident energies in the RIXS plane (red circles, Figure 2.B). Note that cuts

9 in the RIXS map at Constant Incident Energy (CIE) provide resonant X-ray emission spectra. Such spectra

10 correspond to the excitation of close intermediates states (green lines, Figure 2.A) which desexcitation

11 may occurs through different channel giving rise to various final states energies (green lines, Figure 2.A;

12 green circles, Figure 2.B). Hence if discrete excited states are concerned the RIXS map will exhibit vari-

13 ous resonances. Such discrete excited states will necessarily occur in the oxide catalyst because of the

14 strong Coulomb interaction between the electrons in the d-orbitals, as well as (2p,3d) and (3d,3d) ex-

15 change interactions. These on-site electronic interactions induce a splitting in different energies levels[63–

16 65] of the $2p^5 3d^8$ final electronic configuration reached through Co^{II} 1s2p RIXS process. This results in a

17 multiplet structure of Co 1s2p RIXS spectra of CoMo_Al_2O_3_RT catalyst. However due to core-hole

18 lifetimes of the intermediate and the final excited states (Γ_{1s}, Γ_{2p} respectively), the multiplet structure is

19 broadened along the vertical and horizontal axis (see Figure.2 B). [33,35,38] This added to experimental res-

20 olution broadening of excitation energy (0.8 eV), leads to resonances that are not very well resolved with

21 an asymmetrical shape as observed for CoMo_Al_2O_3_RT (figure 1.C). Nevertheless, the multiplet struc-

22 tures could be evidenced through CIE lines as shown in Figure 3. To better understand the origin of the

23 resonances, Kramers- Heisenberg equation[66,67] (eq.1, see experimental section) can be used to calculate

24 Co^{II} 1s2p RIXS plane of CoMo_Al_2O_3_RT. Ω is the frequency of the incident x-ray and ω is the frequency

25 of the outgoing x-ray; D and Q correspond to dipole and quadripole operators, $E_{1s^2 2p^6 3d^7}$, $E_{1s^1 2p^6 3d^8}$ are

1 the energies of ground and intermediate states, Γ_i is the core-Hole lifetime of the intermediate states and

2 L_f indicates the final state Lorentzian broadening. [33,35,38]

3

4

5 $$F(\Omega, \omega) = \sum_f \left[\sum_i \frac{\langle 1s^2 2p^5 3d^8 | D | 1s^1 2p^6 3d^8 \rangle \langle 1s^1 2p^6 3d^8 | Q | 1s^2 2p^6 3d^7 \rangle}{E_{1s^2 2p^6 3d^7} + \Omega - E_{1s^1 2p^6 3d^8} + 1/2 i\Gamma_i} \right]^2 . L_f \, Eq. 1$$
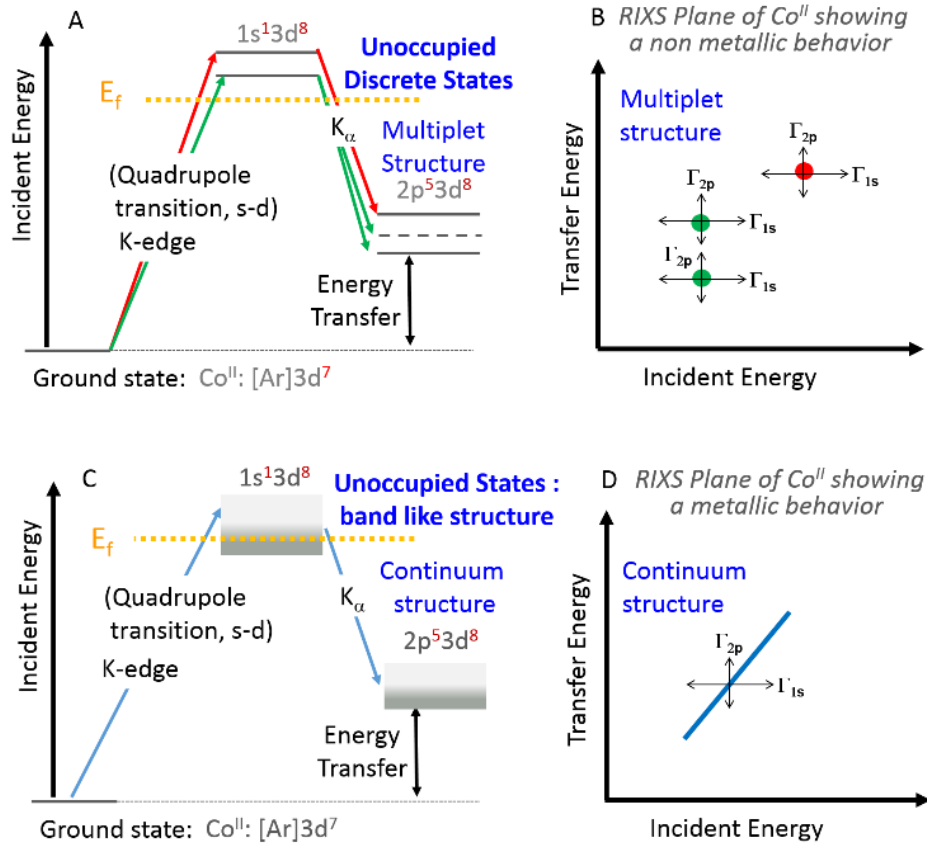
6

7

8 **Figure 2.** Schematic sketch of the RIXS transitions to discrete (A) and continuum (C) excited states to-

9 gether with schematic representation of the expected RIXS maps for discrete (B) and continuum (C) ex-

10 cited states. E_f is the fermi energy level. Adapted from *Glatzel et al*[33,35]

11

1   Based on Eq.1, simulation of RIXS plane of CoMo_Al$_2$O$_3$_RT catalyst is performed by using the crystal

2   field multiplet approach[63,65], as implemented in CTM4XAS and CTM4RIXS softwares.[68] The best agree-

3   ment between experiment and theory is obtained for Co^{II} in octahedral symmetry in high spin configura-

4   tion with a 10 Dq equal to 0.8 eV. A reduction of the Slater integrals and valence spin orbit coupling to

5   90% of their atomic values is required to match the experimental shape. To validate the accuracy of these

6   parameters, CoMo_Al$_2$O$_3$_RT XANES Co L$_{2,3}$ edges spectrum was recorded and the parameters used to

7   calculate the RIXS map have been used to simulate the spectrum. A good agreement between experiment

8   and theory have been obtained as shown in figure S3 of the Supporting Information. Note also that the

9   calculated RIXS map (figure 3.C) was obtained by using higher resolution for the excitation energy (0.3

10 eV) than the experimental one (0.8 eV) in order to better resolve the multiplet structure. This choice of

11 higher resolution simulation parameter is not to investigate deeply multiplet structure of the oxide catalyst

12 since experimental data do not allow it, but to make obvious to the reader the occurrence of multiplet

13 structure for Co^{II} in CoMo_Al$_2$O$_3$_RT. Here, we merely restrict our discussion to show that the of origin

14 of RIXS resonances can be explained by Co^{II} in octahedral symmetry in high spin configuration. Our real

15 purpose at this point, is to shed on light the underlying cause of the change of the resonances RIXS shapes

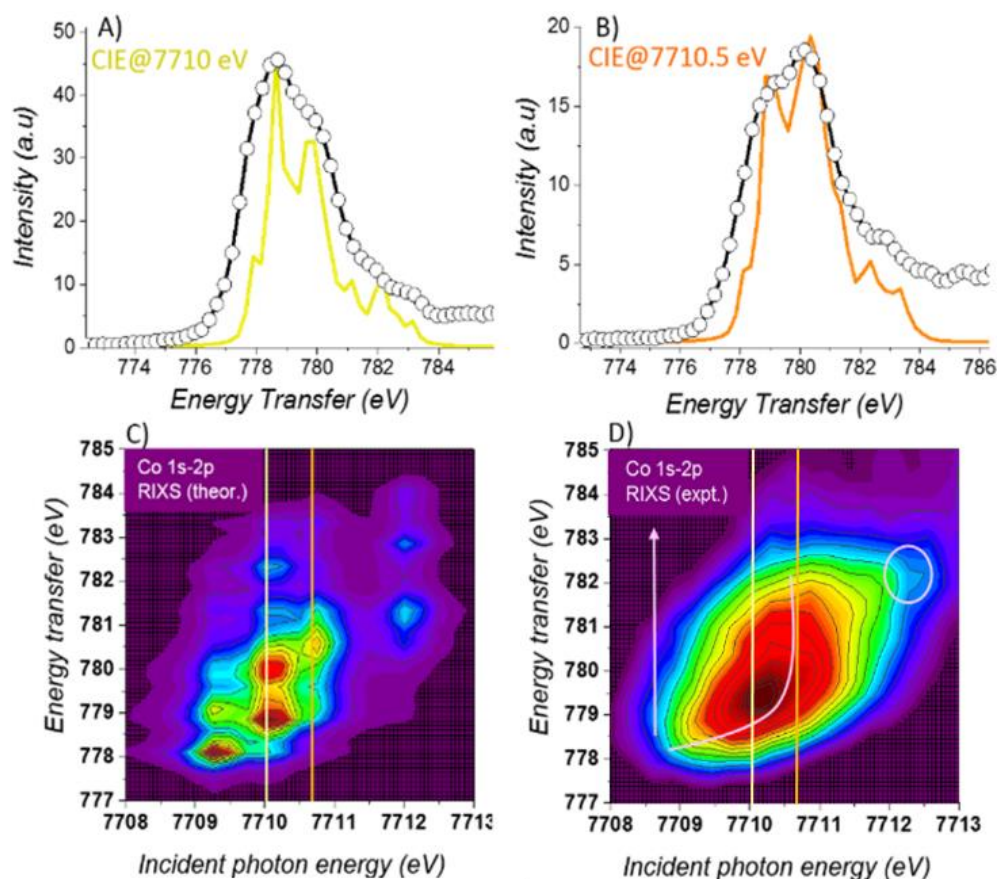16 during the transition from the oxide to sulfide phase.

17

Figure 3. Experimental (dot line) and theoretical (yellow, orange) CIE lines at 7710 eV (A) and 7710. 5 (B) eV together with simulated (C) and experimental (D) Co 1s2p RIXS plane of CoMo_Al2O3_RT catalyst.

Calculations for an octahedral Co^{II} in a high spin configuration shown in Figure.3C show that the pre-edge of CoMo_Al2O3_RT XAS will present three peaks at three incident energies: 7709.3 eV with transfer energy of 778 eV, 7710 eV with energy transfer of 779, 780 and 782.5 eV, 7712 eV with transfer energies at 781 and 783 eV (Figure.3C). As discussed above, such peaks are not well distinguished experimentally due to the low resolution. However, it allows us to explain the asymmetrical shape of the $2p_{3/2}$ resonance RIXS (Figure.3D). In fact, the asymmetrical shape marked by a circle in Fig.3D is due to RIXS resonance at 7712 eV incident energy while the elongation along the vertical originates from three RIXS resonances with energy transfer of 779, 780 and 782.5 eV at 7710 eV incident energy (yellow line

1 fig.3C). The multiplet structure is better evidenced on CIE lines. Indeed, CIE line at 7710 eV extracted

2 from the calculated RIXS map shows a doublet structure (Fig3.A, yellow curve) that is observed experi-

3 mentally (Fig3.A, dotted curve). The CIE line at 7710 eV shows inversion of the doublet intensity com-

4 pared to the CIE line at 7710.5 eV). This is due to the resonances at 781 eV (transfer energy) which

5 exhibits a higher intensity at 7710.0 eV incident energy (Figure.3.C).

6 The RIXS plane of CoMo_Al_2O_3_H_2S (figure 1.d) shows a diagonal elongation with a broadening in the

7 horizontal and vertical directions due to 1s and 2p core lifetimes respectively as it was observed for the

8 oxide catalyst. However, no other asymmetry of the RIXS resonance is observed. Such result is surprising

9 if one considers the Co^{II} final states as $2p^5 3d^8$ configuration as observed for oxide catalyst where a mul-

10 tiplet structure is expected. Here the RIXS plane (Fig. 1d) describes rather excitations to band-like unoc-

11 cupied states (Figure 2 (C, D)). Indeed, the continuous structure of a band in comparison to a discrete

12 states will give rise to continuous resonance feature along the diagonal (figure 2.D) instead of separated

13 resonances (figure 2.B). To confirm this band structure, the RIXS plane of CoMo_Al_2O_3_H_2S_400°C

14 catalyst was simulated by the continuum model[53,69–71] based on equation 2, (see experimental section).

15 where Ω is the frequency of the incident x-ray and ω is the frequency of the outgoing x-ray, E_{Co} is the

16 deep core-level energy and Γ_b the inverse core-Hole lifetime. μ_{XES} and μ_{XAS} are the absorption cross sec-

17 tion and the emission cross section respectively which can be expressed as the X-ray Absorption spectrum

18 and the X-ray Emission spectrum (XES). As shown in Fig.4 a very good agreement between experiment

19 and theory is obtained. The CIE line plots are also well reproduced by calculation.

20

21

$$\sigma(\Omega, \omega) \infty \int \frac{\mu_{XES}(\omega_1) . \mu_{XAS}(\Omega - \omega - \omega_1 + E_{Co})}{\left| \omega - \omega_1 + \frac{\Gamma_b}{2} \right|^2} d\omega_1 \, Eq.\, 2$$
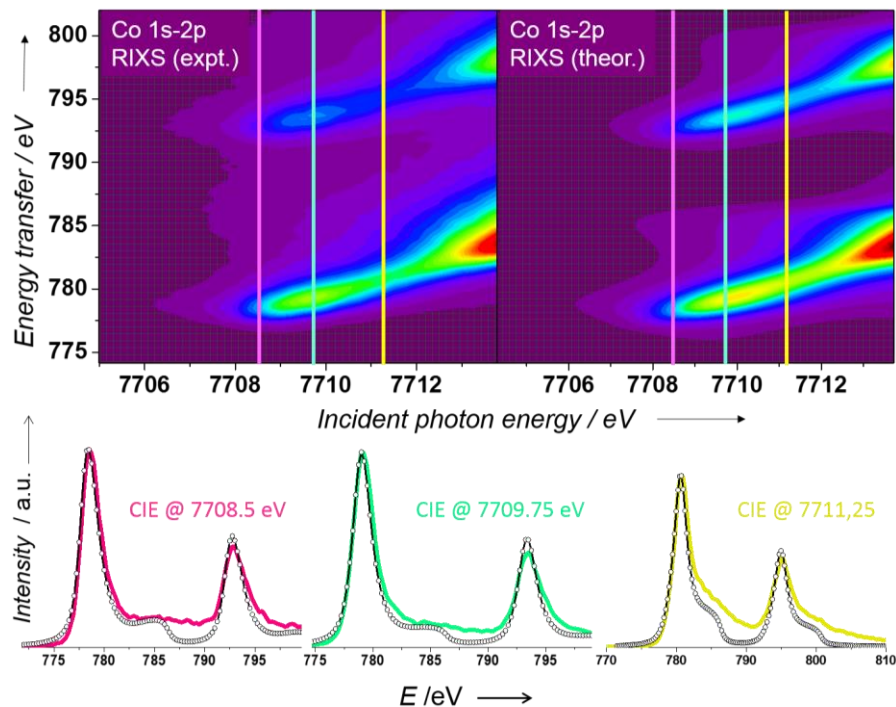
23

1

Figure 4. Experimental and simulated Co 1s2p RIXS plane of CoMo_Al$_2$O$_3$_H$_2$S_ 400°C catalyst to-

gether with theoretical (grey) and experimental (pink, green, yellow) CIE lines at 7708.5, 7709.75 and

7711.25 eV.

Different hypotheses can be suggested to explain excitations to band-like unoccupied states observed for

Co1s2p RIXS plane of CoMo_Al$_2$O$_3$_H$_2$S catalyst. First, multiplet effects should be larger than the ex-

perimental resolution in order to be observed. It is possible that the change of cobalt coordination shell,

under H$_2$S flux, from oxygen ligands to sulfur ones, gives rise to less separated multiplet peaks that could

not be resolved within our experiment. However, the absence of any asymmetry on RIXS features make

this hypothesis unlikely. Second, edge calculation within the frame of Kramers-Heisenberg equation

(Eq.1) describes a local quadrupole transition. The pre-edge of CoMo_Al$_2$O$_3$_H$_2$S catalyst could present

a dipolar contribution (1s → p-band) dominating the quadrupolar one.[58] Last hypothesis to explain the

peculiar structure of the sulfide RIXS map is to take into account excitations to band-like unoccupied d-

states revealing a metallic character of Co (figure 2.c-d). Such a metallic character is consistent with the

1   results obtained for model HDS catalysts and DFT calculations [25,26]. However, to the best of our

2   knowledge, it has never been reported for "real" catalysts. X-ray Photoelectron Spectroscopy (XPS) and

3   K$\beta_{1,3}$ X-ray emission spectroscopy (XES) will be used to provide additional evidences of this metallic

4   character.

5   Earlier XPS data processing published in the literature for HDS catalysts use nonmetallic fitting parame-

6   ters. [39,41,42,72] Fig.5 shows CoMo_Al$_2$O$_3$_H$_2$S XPS Co2p spectrum adjusted according to the method usu-

7   ally used in the literature.[39,41,42,72] This method consists on fitting the Co2p spectral envelope of a oxidic

8   precursor of the catalyst. These oxide contributions are then introduced in the spectrum of a monometallic

9   (Co) sulfided catalyst, while maintaining the extracted constraints for Co oxide fixed (Binding Energies:

10 BE, Full Width at Half Maximum : FWHM, and area ratios; as well as the FWHM ratio of the Co2p main

11 peak to the Al2p peak). The Co$_9$S$_8$ spectral envelope is deduced from the difference between the cobalt

12 sulfide sample global envelope and the Co oxide contributions. The CoMoS phase Co2p spectral envelope

13 is finally deduced from the difference between a bimetallic catalyst Co2p spectral envelope and the two

14 aforementioned Co oxide and Co$_9$S$_8$ spectral contributions. Following this methodology, three conven-

15 tional spectral shape were used to fit the CoMo_Al$_2$O$_3$_H$_2$S catalyst Co2p envelope: Co$_9$S$_8$, CoMoS and

16 Co^{II} oxide phases. The main Co2p$_{3/2}$ peak of cobalt atoms within in these three phases lie respectively at

17 778.2 eV, 778.7 eV and 781.2 eV. Based on the above described decomposition of the XPS spectra, we

18 determined the relative concentrations of each Co species. A proportion of only 39 % of Co in CoMoS

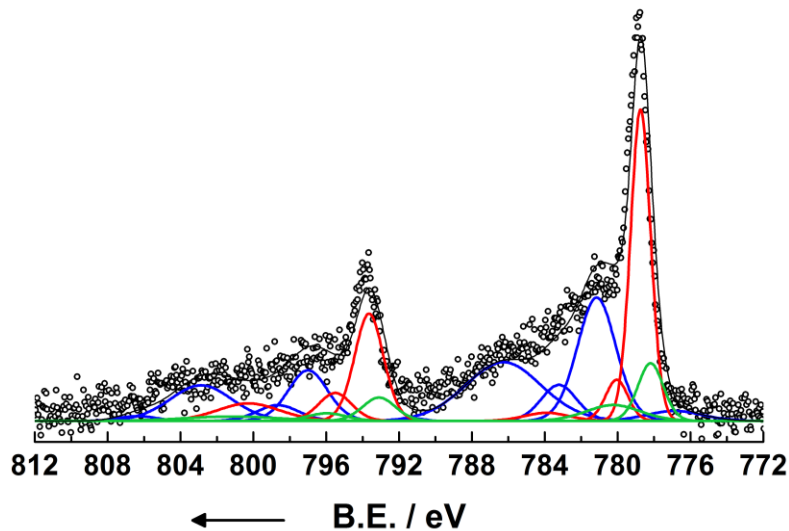19 phase is obtained, while the percentage of remaining Co oxide is equal to 49%.

20

Figure 5. XPS Co 2p spectrum of the CoMo_Al$_2$O$_3$_H$_2$S catalyst. The decomposition previously re-ported in the literature is applied here (blue: Co^{2+} oxide contributions; green: Co$_9$S$_8$ contributions; red: CoMoS contributions).

Figure 6 now presents the same Co 2p$_{3/2}$ XPS spectrum for CoMo_Al$_2$O$_3$_H$_2$S sample compared to the Co 2p3/2 XPS spectrum of a clean cobalt sulfide Co$_9$S$_8$ reference sample, which is known to be metallic.[73] The high-resolution spectrum for Co$_9$S$_8$ presents a distinct asymmetric line shape that has already been observed previously.[74] This asymmetrical shape can be explained by the metallic behavior of this com-pound.[75,76] Indeed, due to unfilled electron levels above the Fermi energy, shake-up-type events following core electron photoionization exist and are responsible for a tail at the high binding energy side of the core photoelectron peak.[77] Co$_9$S$_8$ spectrum was thus fitted following the decomposition proposed for Co metal and Co phosphide,[52] with an asymmetric main peak with binding energy of 778.1 eV, FWHM value of 0.8 eV and two plasmon loss peaks at 3.0 eV and 5.0 eV above the main peak, which constitute the surface and bulk plasmons, respectively, with FWHM values of 3.3 eV in both cases.[52,53] The metallic character of this compound is also highlighted in this work with XPS valence Band (VB) showing a sharp edge localized at the Fermi level (Figure 6.C).
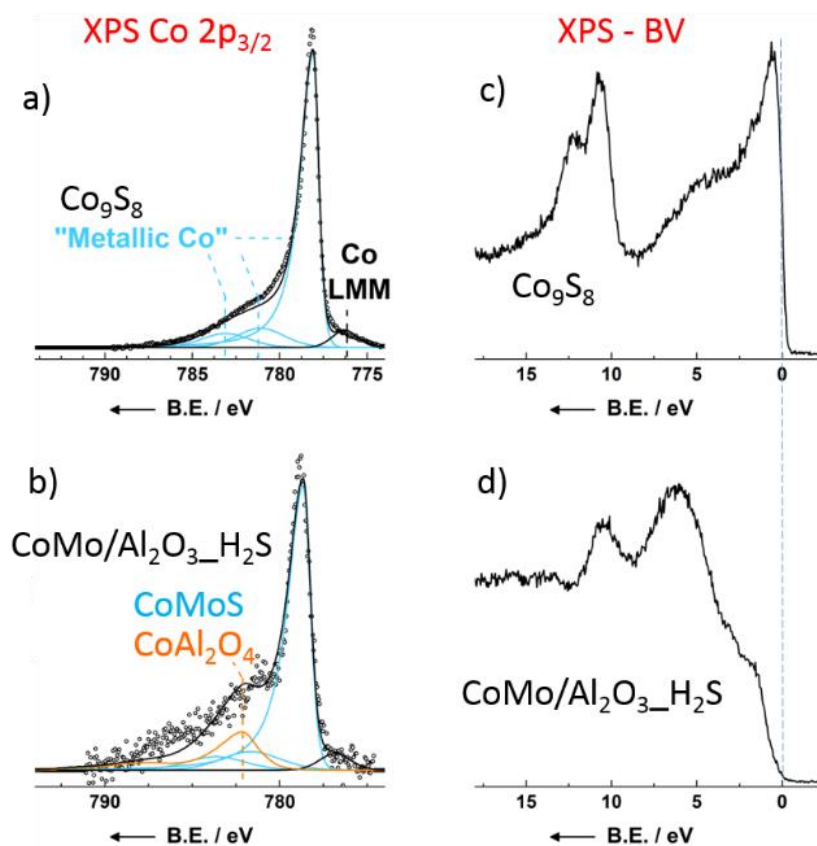
1

Figure 6. XPS Co 2p3/2 spectrum of a) Co_9S_8 reference and b) $CoMo\_Al_2O_3\_H_2S$ catalyst, XPS-VB of c) Co_9S_8 reference and d) $CoMo\_Al_2O3\_H_2S$ catalyst

The $CoMo\_Al_2O_3\_H_2S$ catalyst VB (figure 6.D) shows an edge localized at the Fermi level, confirming its metallic behavior. However, the VB is largely dominated by MoS_2 and alumina bands (Supporting Information (Figure S4)), making the determination of the electronic state of cobalt difficult. Neverthe-less, Co $2p_{3/2}$ orbital shape of $CoMo\_Al_2O_3\_H_2S$ is very similar to the one of Co_9S_8. This shape together with excitations to band-like unoccupied states shown by RIXS measurements, support the use of Co metal parameters to fit $Co2p_{3/2}$ peak (Fig.6b). The main peak corresponding to Co atoms involved in CoMoS phase lies at 778.6 eV with a FWHM value of 0.9 eV. This small value of FWHM is close to the bulk Co_9S_8 reference one, suggesting the presence of only one sulfide Co phase in $CoMo\_Al_2O_3\_H_2S$

1   sample. It is however possible to add a small proportion of Co_9S_8 phase (maximum 10 %) in the decom-

2   position even if the CoMoS and the Co_9S_8 Co2p main peak are separated by 0.5 eV. Finally, the fitting

3   requires addition of Co^{II} oxide contribution. This contribution is responsible for 20 % of the total Co $2p_{3/2}$

4   orbital.

5   The new XPS fitting, proposed in this work, explains the discrepancy of the results concerning the quan-

6   tification of cobalt sulfidation rate by XAS and XPS (sulfidation rate between 40 and 60% by XPS process

7   while XAS show an almost total sulfidation). As shown above, processing XPS data implies fitting the

8   catalyst spectral shape of the various contributions of Co species through the decomposition of the exper-

9   imental spectra by mathematical functions showing adjustable fitting parameters (FWHM, peak posi-

10   tion... etc). The accuracy of fitting parameters depends on the precise knowledge of the electronic struc-

11   ture of the probed element (multiplet structure, metallic structure, plasmons...). In the present work we

12   used Co 1s2p RIXS to probe the electronic structure cobalt that suggest the use of metallic parameters

13   fitting to adjust the experimental XPS spectra. This new fit moves the ratio Co^{II} oxide/Co^{II} sulfide from

14   50%/50% to 20%/80% (see table 1). This ratio eventually allows to reach an agreement between XPS and

15   XAS spectroscopies quantification.

16   Taking into account the correct electronic structure for Co, raises a Co-promotion rate (Co/Mo atomic

17   ratio) issue. Indeed, in HDS community, the cobalt promotion rate is determined based on Co 2p and Mo

18   3d XPS spectra. Figure 7 show XPS Mo 3d spectrum of CoMo_Al_2O_3_H_2S catalyst. The Mo 3d envelope

19   can be adjusted by the spectral contributions of $Mo^{IV}S_2$ (75%) and Mo^{VI} oxide (25%). Contributions of

20   S_{2s} should be added as this latter is overlapping with the Mo 3d (5/2) of the $Mo^{IV}S_2$. Using previous fit

21   from the literature and the new fit proposed in this work, the Cobalt involved in the CoMoS phase is equal

22   to 39% and 80% respectively (table 1). This gives a Co/Mo atomic ratio in the CoMoS phase equal to

23   0.46 (actual fit) and 0.31 (previous fit). Consequently, Co-promotion rates available in literature seems

24   underestimated and should be reevaluated for a proper correlation to HDS activity. This questions the

1 strategy of trying to increase a Co-promotion rate (already very high), and suggests that synthesis route

2 increasing the amount/size/dispersion of the CoMoS active phase may be more useful.

3

4

5
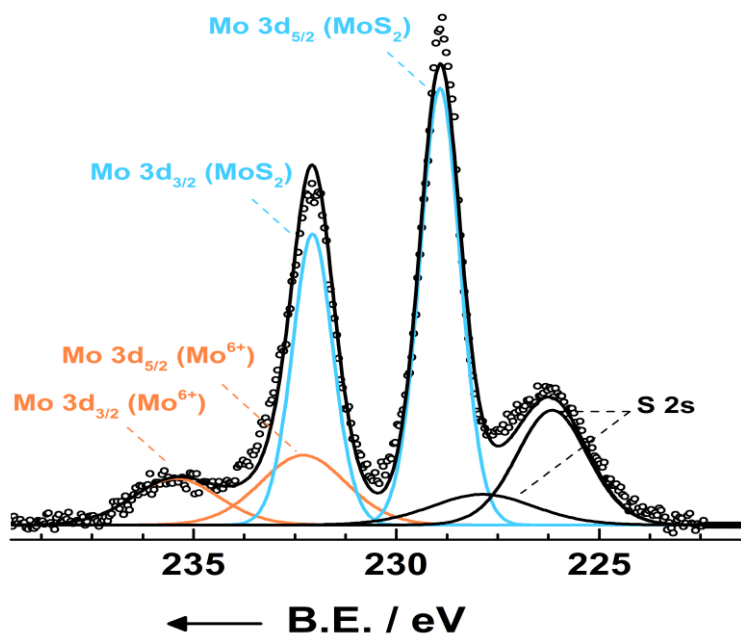
6 **Figure 7.** XPS Mo 3d spectrum of CoMo_Al_2O_3_H_2S catalyst

7

8

	Co(II) oxide	CoMoS phase	Co_9S_8 phase
Literature	49	39	12
This work	20	80	0

9 **Table 1.** XPS at. % of the different Co phases contributions obtained for CoMo_Al_2O_3_H_2S catalyst

10 using decomposition from literature and from this work.

Geometric structure of cobalt centers in HDS catalysts. HERFD-XAS and XES have been used to monitor the genesis of the CoMoS active phase and to resolve the local environment of cobalt. The catalyst was heated up to 400 °C in a ramp of 1 °C/min under a flux of H_2/H_2S (10% H_2S). Fig.8b show Co $K\beta_{1,3}$ emission lines of CoMo_Al_2O_3 catalyst recorded at room temperature (CoMo_Al_2O_3_RT) under air flux and at 400°C under H_2/H_2S flux (CoMo_Al_2O_3_H_2S). The $K\beta$ fluorescence line is observed after photoionization of a 1s electron. After photon absorption, 1s core hole is filled by relaxation of a 3p electron. This relaxation process is at the origin of the $K\beta$ emission. The shape of the Co $K\beta$ line consists of one main peak at high fluorescence energy ($K\beta_{1,3}$) and a "satellite structure" denoted as $K\beta'$ at low fluorescence energy. This latter is due to the (3p, 3d) exchange interaction and is therefore highly sensitive to the valence spin density.[38] Fig.9 show a schematic sketch of the process involved in the $K\beta$ emission line. The photoionization involves a spin down and spin up transitions (red arrows Figure 9). The relaxation process will therefore present two decay channels corresponding to spin down and spin up desexcitation (green arrows, Figure 9).[78] The electronic state of Co^{II} reached through a spin down desexcitation is ^5G, while it is ^3G for the spin up transition (Figure.9). After the sulfudation, the $K\beta_{1,3}$ peak of CoMo_Al_2O_3_H_2S_400°C is shifted about 1 eV to higher energies with respect to CoMo_Al_2O_3_RT together with a vanishing of Co $K\beta'$ structure at 7638 eV as denoted in Figure.8B. The vanishing of Co $K\beta'$ structure account for a major change of the spin state of the HDS catalyst during the sulfidation step. This change is again related to the Cobalt metallic character giving rise to non-distinguishable collective valence electrons: only one 3p-1s channel decay is observed as $K\beta'$ merges into $K\beta_{1,3}$ main line as shown in Figure.8B.[79] This metallic character will allow us to make site selective measurements that one may think unlikely. Indeed, the promoter in both the sulfide and oxide phases show the same oxidation state (+II). Therefore, and if the metallic nature of the promotor is not considered, no significant energy shift of emission lines is expected during the catalyst activation. Thanks to the global change of the electronic structure a shift of the order of 1 eV is observed making possible site selective XAS study to discriminate between oxide (Co^{II}-O) and sulfide (Co^{II}-S) phases arising during the catalyst activation. However, since

1 the $K\beta_{1,3}$ peaks of (Co-O) and (Co-S) species are overlapping (figure 8.b), only partial selective HERFD-

2 XAS spectra are obtained by measuring directly the XAS spectra at a given spectrometer energy. To

3 achieve total selectivity, a deconvolution of experimental spectra recorded for two emission energies of

4 the spectrometer is required. For this purpose, the spectrometer was aligned at two energies, *i.e.,* 7651.1

5 eV, with $K\beta_{1,3}$ (Co-O) /(Co-S) intensity ratio equal to 2 (Figure 8.c), and 7649.3 eV with $K\beta_{1,3}$ (Co-O) /

6 (Co-S) ratio equal to 0.85 (Figure 8.a). The recorded HERFD-XAS for each of these two energies ($S_{@7649.3}$

7 and $S_{@7651.1}$) can be written as a linear combination of the pure spectrum of the oxide phase (S_{ox}) and the

8 sulfide phase (S_{sul}). This gives rise to a system of two equations (equations 3 and 4) with two variables

9 (S_{ox} and S_{sul}). γ_{ox} and γ_{sul} are the fraction of the oxide and the sulfide respectively, corrected by (Co-O) /

10 (Co-S) ratio rising form the energy of the spectrometer. γ_{ox} and γ_{sul} fractions where obtained based on

11 XPS fitting of the Co 2p envelope as discussed above.

12

$$13 \quad S_{@7649,3eV} =$$

$$14 \quad \gamma_{ox@7649,3eV} \cdot S_{ox} + \gamma_{sul@7649,3eV} \cdot S_{Sulf} \, Eq.\, 3$$

15

$$16 \quad S_{@7651,1eV} =$$

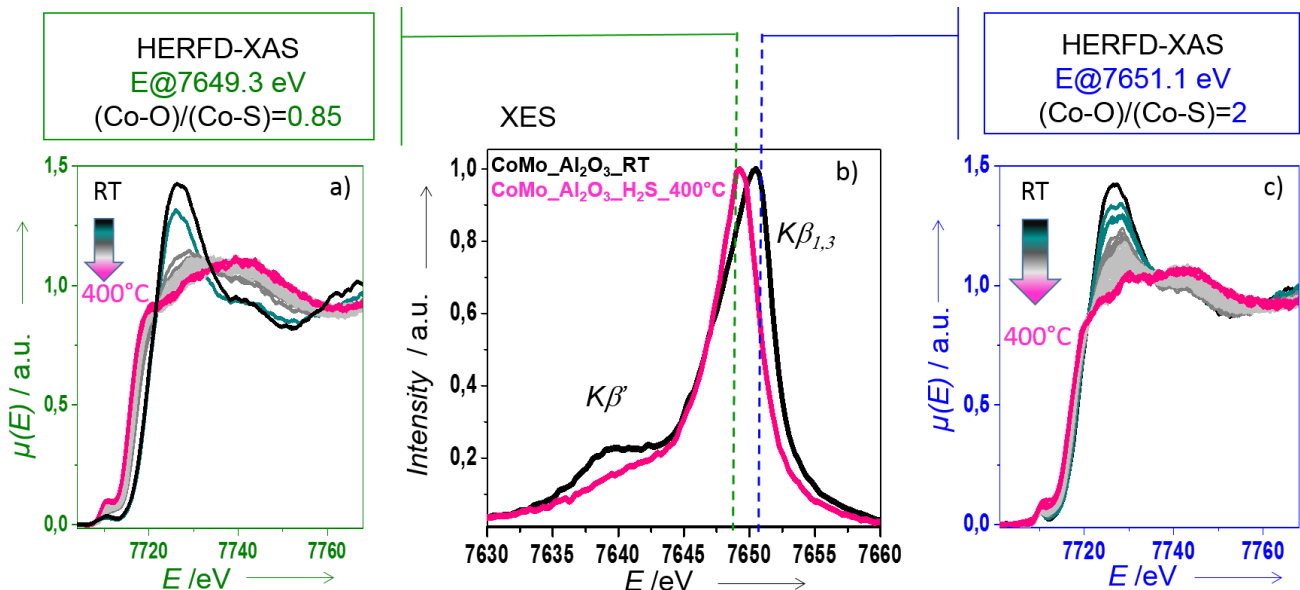$$17 \quad \gamma_{ox@7651,1eV} \cdot S_{ox} + \gamma_{sul@7651,1eV} \cdot S_{Sulf} \, Eq.\, 4$$

18

Figure 8. S@7649.3 (a) and S@7651.1 (c) HERFD-XAS spectra recorded during CoMo_Al₂O₃ catalyst activation, Co K$\beta_{1,3}$ emission lines (b) of the alumina supported CoMo catalyst recorded at room temperature (black curve) under air flux and at 400°C under H_2/H_2S flux (pink curve).

Fig 8.a and Fig 8.c show that before introducing the gas, an intense white line (wl) is observed (black curve) which is the signature of Co^{II} oxide in octahedral symmetry. At 400°C the wl is missing (pink curve, Fig 8. a and Fig8.c), illustrating that almost all of the initial oxide is converted to sulfide species in agreement with RIXS and XPS spectroscopies. Recording the spectra at a detection energy of 7651.1 eV where the (Co-O)/(Co-S) intensity ratio is equal to 2, will select the XAS signal of the oxide species. At a detection energy of 7649.3 eV ((Co-O)/(Co-S) intensity ratio equal to 0.85) the sulfide species XAS signal will be selected. This evidenced on S$_{@7649.3}$ spectra (Fig 8a.) where the wl is vanishing right after introduction of the gas. A shift to lower energy is also observed. S$_{@7651.1}$ spectra (Figure.8c) follows the same trend but is much smoother. This clearly shows that, from the experimental point of view, it is possible to be more sensitive to oxide or sulfide species by choosing the appropriate spectrometer energy. Regarding the access to pure spectra of oxide and sulfide, Eq.3 and Eq.4 should be applied. However, the

1 results obtained with such an approach are limited, insofar only part of the XANES signal might be used

2 for structural investigation of the catalyst active site. Indeed, HERFD-XAS spectra are recoded by fixing

3 one detection energy (emission energy) while scanning the excitation energy through the Co K absorption

4 edge, leading to the detection of only a fraction of electronic excited states, while, in "classical" XAS,

5 pre-edge structure corresponds to the sum of these states. It follows that any interpretation of the pre-edge

6 structure of HERFD-XAS spectra is improper.[32,33] Therefore, neither intensity nor the structure of the pre-

7 dege is considered and only the global shape of the HERFD-XAS spectra will be discussed. Note that

8 even XANES features are modified as function of the selected emission energy due to lifetime broadening

9 distortions and spin configurations.[78] Indeed, as discussed above, $K\beta_{1,3}$ and $K\beta'$ peaks result from two

10 different spin configurations. It is therefore possible to record spin-dependent XAS spectra by fixing emis-

11 sion energy at the main peak ($K\beta_{1,3}$) and at the satellite ($K\beta'$) while scanning the incident energy.[80] The

12 two emission energies fixed in this work are very close and fall into the region of the main emission peak

13 ($K\beta_{1,3}$). These two emission energies were used to record Co K edge XAS references Co^{II} oxides com-

14 pounds and no change of the XAS shape was observed in agreement with previous results.[32,79]
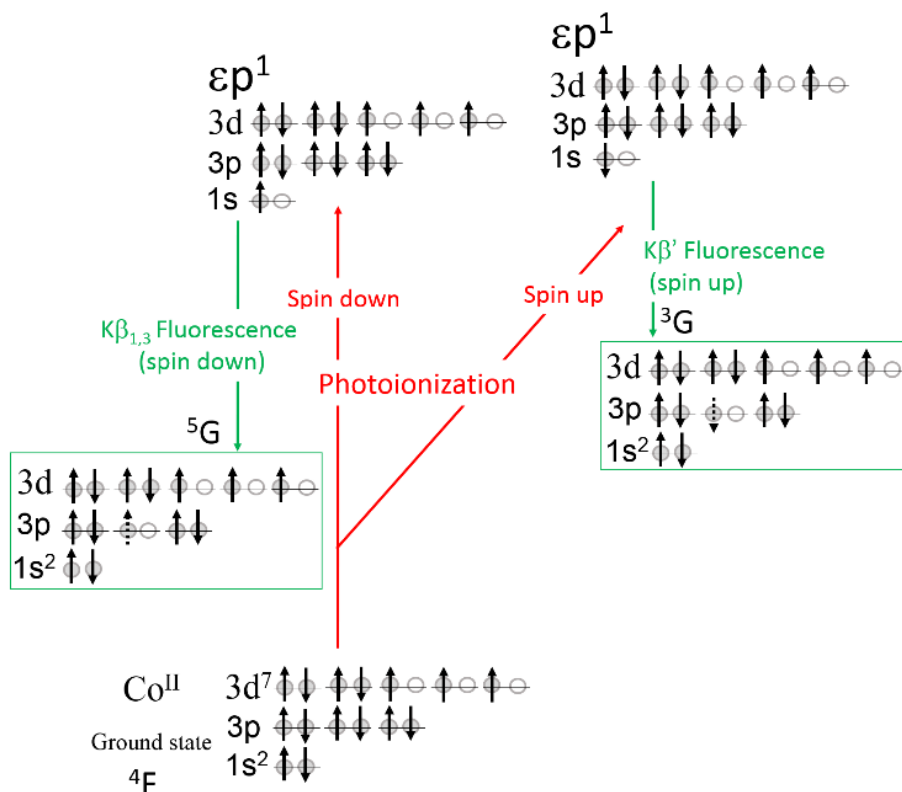
15

Figure 9. A schematic sketch of the process involved in the K_β emission line for the Co^{II} configuration.

Based on Eq.3 and Eq.4, pure ligand-specific Co K edge HERFD-XAS spectra are extracted (figure 10). Note that from RT to 50°C, the shape of the spectra evolves very quickly and the spectra were too noisy to be used. From 50°C, the spectra evolution is smooth and it becomes possible to lower signal-to-noise ratio by merging analogous spectra before deconvolution. From T= 50 to 216°C, the extracted S_{ox} spectra (figure 10, blue curve) show a split up and a decrease of wl intensity. This is due to a mixture of Co^{II} in octahedral symmetry with tetrahedral cobalt aluminate species. Indeed, it is well known that Co^{II} shows a high affinity to empty tetrahedral sites of the spinel γ-alumina oxide support leading to the formation of cobalt aluminate during synthesis steps.[81] The activation of the catalyst converts only octahedral oxide Co^{II} to sulfide species while the cobalt aluminate remains in its oxide state. This is consistent with the
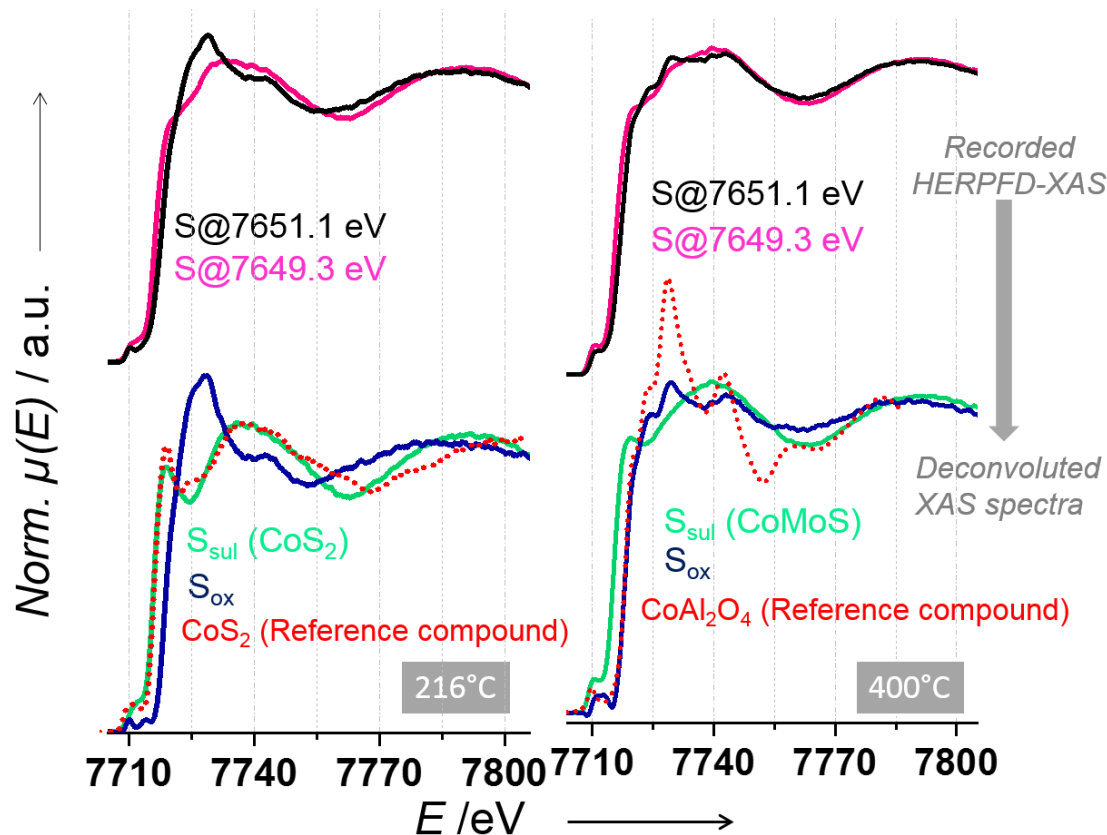
1 observation of cobalt aluminate features only for S_{ox} at T= 400°C (Fig.10, blue curve). This is also con-

2 sistent with XPS results discussed above in the article and showing that the fitting of the total Co $2p_{3/2}$

3 orbital requires besides the cobalt sulfur phase, the addition of a tetrahedral Co^{II} oxide ($CoAl_2O_4$) contri-

4 bution. Note that the wl of S_{ox} at T= 400°C (Fig.10, blue curve) is less intense for S_{ox} than for the $CoAl_2O_4$

5 reference compound (Fig.10, purple curve). Indeed, the pure XAS spectrum of cobalt inserted in empty

6 tetrahedral sites of the spinel γ-alumina is unknown, nevertheless such XAS spectrum is expected to show

7 similar features to the one of $CoAl_2O_4$ reference compound due to the same symmetry and chemical en-

8 vironment of Co in both case. For the catalyst, the cobalt shows high dispersion in contrast to the $CoAl_2O_4$

9 bulk reference compound.

10

11

12 **Figure 10**. HERFD-XAS S@7649,3eV and S@7651,1eV spectra and their corresponding deconvoluted

13 S_{ox} and S_{sul} spectra for two temperatures ranges together with CoS_2 and $CoAl_2O_4$ references compounds

1

2 From T= 50 to 216°C, the extracted S_{sul} (green curve, Fig.10) show spectrum fingerprints similar to CoS_2

3 compound (purple curve, Fig.10).To the best of our knowledge, the formation of CoS_2 as HDS catalyst's

4 activation intermediate has never been reported in the literature. A Co monometallic catalyst (without

5 Mo) also shows CoS_2 formation upon exposure to H_2/H_2S mixture (Supporting Information (figure S5-

6 1)). At higher temperature, CoS_2 is converted to thermodynamically stable Cobalt sulfide phase Co_9S_8

7 (Supporting Information (figure S5-2)).) while XANES spectra of the bimetallic catalyst show new fea-

8 tures that may be related to the genesis of CoMoS phase (Fig. 2, T= 400°C, green curve).

9 Thanks to the partial fluorescence detection and to the removal of cobalt aluminate form the global signal,

10 XANES spectrum of CoMoS shows sharper features compared to those published in the literature making

11 comparison to theoretical XANES spectra possible. CoMoS structures showing S/M-edges were gener-

12 ated by DFT calculation and their corresponding Co K edge XANES spectra were calculated (Fig 11). Co

13 located at S-edges show tetrahedral symmetry while Co located M-edges are square planar (D_{4h}) in agree-

14 ment with previous DFT results. [16] In the D_{4h} configuration, Co 4p-orbitals are split into A_{2u} and E_u sym-

15 metries. The latter overlap with E_u sulfur p-orbitals, whereas A_{2u} Co 4p-orbitals remain non-binding. This

16 gives rise to a shoulder at 7715 eV due to electron transition to the non-bonding A_{2u} for D_{4h} symmetry

17 (Fig 11). This shoulder is missing for tetrahedral Cobalt as its p-orbitals are degenerate. No shoulder is

18 observed for S_{sulf} HERFD XAS spectrum of the CoMoS phase. This absence and the dissimilarity of

19 global spectrum shape between theoretical Co M-edges spectrum and the experimental one, rules out a

20 Co square plane symmetry. S_{sul} spectrum exhibits characteristics similar to the theoretical XANES Co S-

21 edges (tetrahedral symmetry) indicating that the Co substitution at the CoMoS edges seems to occur

22 mainly at the S-edges. Nevertheless, location of the promotor on defect sites as well the presence of S

23 vacancies will generate multiple Co's in similar local coordination (tetrahedral symmetry). Based on

24 HERFD XANES spectra, only information regarding the local coordination of the cobalt can be drawn

1 from our data. Therefore, it cannot be ruled out that some of the cobalt with tetrahedral symmetry is

2 located close to S-vacancies and/or on defects sites.

3
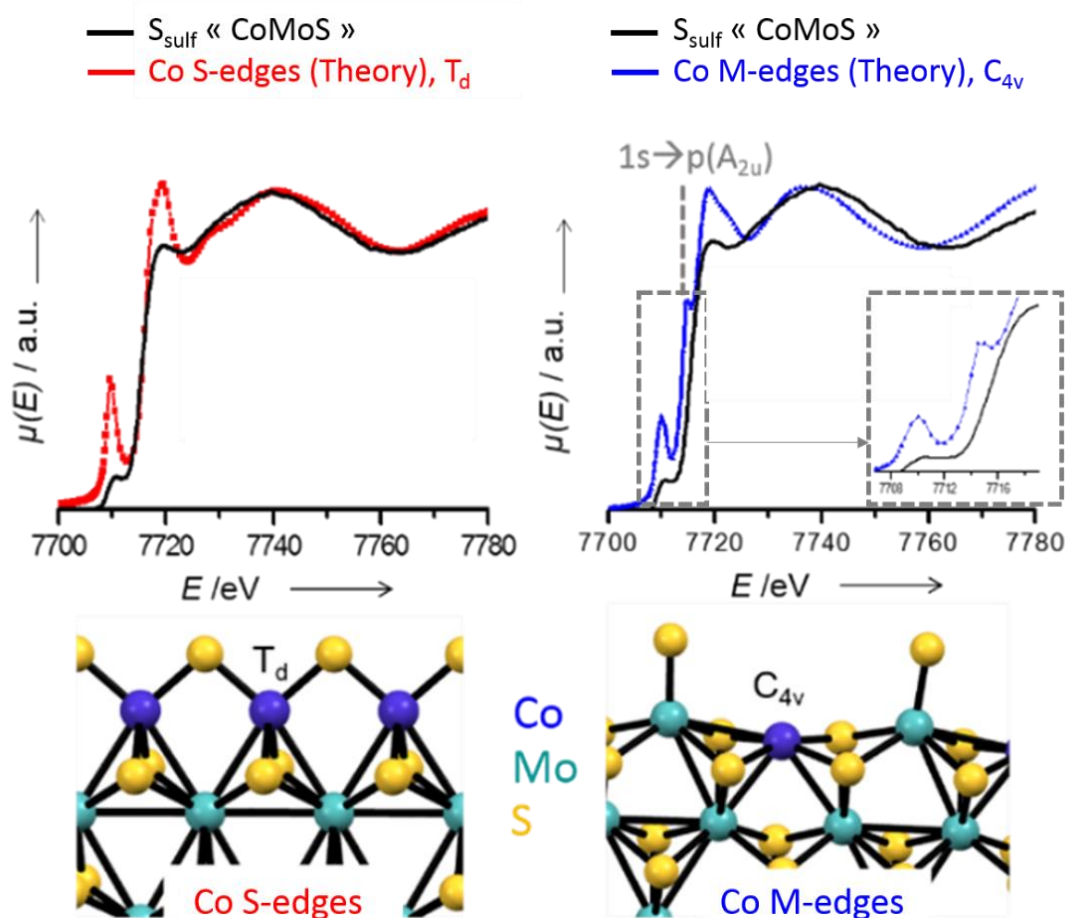
5 **Figure 11.** S_{sulf} CoMoS HERFD XAS compared to theoretical Co K edge XANES spectra for Co S-

6   edges and M-edges together with Co S and M edges after geometry optimization of the CoMoS struc-

7   ture.

8 Conclusion

9 We have shown that $K\beta_{1,3}$-HERFD-XAS and 1s2p RIXS are very powerful to characterize both electronic

10 and geometric structure of TMSs heterogeneous catalysts active sites. These spectroscopies will play a

11 key role throughout the design and the improvements of the TMS's catalysts formulation. For HDS cata-

12 lysts, these techniques made possible the localization of Co in HDS catalysts (S-edge substitution) which

is in line with previous STM and DFT results obtained for model HDS catalysts. These findings pave the way to future investigations on the impact of Co S/M-edges substitution on the final properties of the catalyst allowing a deeper understanding of the catalytic activity and a more efficient HDS catalysts design. The application of Co 1s2p RIXS, XPS and Co $K\beta_{1,3}$ XES spectroscopies shed light on the metallic character of Co in the CoMoS phase for "real" HDS catalysts explaining the reason of the disagreement between sulfidation degree obtained by XPS and XAS reported in the literature. This is questioning the Co promotion rate which seems to be often underestimated and should be reconsidered for a better correlation with the catalytic activity.

ASSOCIATED CONTENT

Supporting Information

A photography of the experimental set up used for *in situ* Co K edge HERFD XAS and Co 1s2p RIXS measurements; theoretical and experimental CoMo_Al$_2$O$_3$_RT XANES Co L$_{2,3}$ edges spectra; Valence Band of MoS$_2$ and γ-alumina; details of synthesis and Co K edge HERFD XAS Characterization of monometallic Co catalyst (Co_Al$_2$O$_3$).

The Supporting Information is available free of charge (PDF).

AUTHOR INFORMATION

Corresponding Author

sylvain.cristol@univ-lille.fr, asma.tougerti@univ-lille.fr

Author Contributions

The manuscript was written through contributions of all authors. All authors have given approval to the final version of the manuscript. ‡These authors contributed equally. (match statement to author names with a symbol)

REFERENCES

(1)   Steinlechner, C.; Roesel, A. F.; Oberem, E.; Päpcke, A.; Rockstroh, N.; Gloaguen, F.; Lochbrunner, S.; Ludwig, R.; Spannenberg, A.; Junge, H.; et al. Selective Earth-Abundant System for CO$_2$ Reduction: Comparing Photo- and Electrocatalytic Processes. *ACS Catal.* **2019**, *9* (3), 2091–2100. https://doi.org/10.1021/acscatal.8b03548.

(2)   Nikodinoska, N.; Cesaro, L.; Romano, R.; Paletto, A. Sustainability Metrics for Renewable Energy Production: Analysis of Biomass-Based Energy Plants in Italy. *J. Renew. Sustain. Energy* **2018**, *10* (4). https://doi.org/10.1063/1.5022659.

(3)   Chen, Z.; Zhang, H.; Guo, P.; Zhang, J.; Tira, G.; Kim, Y. J.; Wu, Y. A.; Liu, Y.; Wen, J.; Rajh,

T.; et al. Semi-Artificial Photosynthetic CO_2 Reduction through Purple Membrane Re-Engineering with Semiconductor. *J. Am. Chem. Soc.* **2019**, *141* (30), 11811–11815. https://doi.org/10.1021/jacs.9b05564.

(4)   Shi, Y.; Zhou, Y.; Yang, D.-R.; Xu, W.-X.; Wang, C.; Wang, F.-B.; Xu, J.-J.; Xia, X.-H.; Chen, H.-Y. Energy Level Engineering of MoS2 by Transition-Metal Doping for Accelerating Hydrogen Evolution Reaction. *J. Am. Chem. Soc.* **2017**, *139* (43), 15479–15485. https://doi.org/10.1021/jacs.7b08881.

(5)   Holzhäuser, F. J.; Mensah, J. B.; Palkovits, R. (Non-)Kolbe Electrolysis in Biomass Valorization- a Discussion of Potential Applications. *Green Chem.* **2020**, *22* (2), 286–301. https://doi.org/10.1039/c9gc03264a.

(6)   Zhu, C.; Fu, S.; Shi, Q.; Du, D.; Lin, Y. Single-Atom Electrocatalysts. *Angew. Chemie - Int. Ed.* **2017**, *56* (45), 13944–13960. https://doi.org/10.1002/anie.201703864.

(7)   Foit, S. R.; Vinke, I. C.; de Haart, L. G. J.; Eichel, R. Power-to-Syngas: An Enabling Technology for the Transition of the Energy System? *Angew. Chemie - Int. Ed.* **2017**, *56* (20), 5402–5411. https://doi.org/10.1002/anie.201607552.

(8)   Zhang, J.; Wang, X. Solar Water Splitting at Λ=600 Nm: A Step Closer to Sustainable Hydrogen Production. *Angew. Chemie - Int. Ed.* **2015**, *54* (25), 7230–7232. https://doi.org/10.1002/anie.201502659.

(9)   Wang, J.; Xi, J.; Wang, Y. Recent Advances in the Catalytic Production of Glucose from Lignocellulosic Biomass. *Green Chem.* **2015**, *17* (2), 737–751. https://doi.org/10.1039/c4gc02034k.

(10) Huber, G. W.; Corma, A. Synergies between Bio- and Oil Refineries for the Production of Fuels from Biomass. *Angew. Chemie - Int. Ed.* **2007**, *46* (38), 7184–7201. https://doi.org/10.1002/anie.200604504.

(11) *Refinery Catalysts Market, Global Trends and Forecasts to 2019 (Market Research Report),*; 2019.

(12) Furimsky, E. Catalytic Hydrodeoxygenation. *Appl. Catal. A Gen.* **2000**, *199* (2), 147–190. https://doi.org/10.1016/S0926-860X(99)00555-4.

(13) Li, X.; Chen, G.; Liu, C.; Ma, W.; Yan, B.; Zhang, J. Hydrodeoxygenation of Lignin-Derived Bio-Oil Using Molecular Sieves Supported Metal Catalysts: A Critical Review. *Renew. Sustain. Energy Rev.* **2017**, *71*, 296–308. https://doi.org/10.1016/j.rser.2016.12.057.

(14) Bachrach, M.; Marks, T. J.; Notestein, J. M. Understanding the Hydrodenitrogenation of Heteroaromatics on a Molecular Level. *ACS Catal.* **2016**, *6* (3), 1455–1476. https://doi.org/10.1021/acscatal.5b02286.

(15) Guo, Y.; Park, T.; Yi, J. W.; Henzie, J.; Kim, J.; Wang, Z.; Jiang, B.; Bando, Y.; Sugahara, Y.; Tang, J.; et al. Nanoarchitectonics for Transition-Metal-Sulfide-Based Electrocatalysts for Water Splitting. *Adv. Mater.* **2019**, *31* (17), 1807134. https://doi.org/10.1002/adma.201807134.

(16) Grønborg, S. S.; Salazar, N.; Bruix, A.; Rodríguez-Fernández, J.; Thomsen, S. D.; Hammer, B.; Lauritsen, J. V. Visualizing Hydrogen-Induced Reshaping and Edge Activation in MoS2 and Co-Promoted MoS2 Catalyst Clusters. *Nat. Commun.* **2018**, *9* (1). https://doi.org/10.1038/s41467-018-04615-9.

(17) Chandra Srivastava, V. An Evaluation of Desulfurization Technologies for Sulfur Removal from Liquid Fuels. *RSC Adv.* **2012**, *2* (3), 759–783. https://doi.org/10.1039/C1RA00309G.

(18) Kaluža, L.; Palcheva, R.; Spojakina, A.; Jirátová, K.; Tyuliev, G. Hydrodesulfurization NiMo Catalysts Supported on Co, Ni and B Modified Al2O3 from Anderson Heteropolymolybdates. *Procedia Eng.* **2012**, *42*, 873–884. https://doi.org/10.1016/J.PROENG.2012.07.480.

(19) Mazurelle, J.; Lamonier, C.; Lancelot, C.; Payen, E.; Pichon, C.; Guillaume, D. Use of the Cobalt

Salt of the Heteropolyanion [Co2Mo10O38H4]6– for the Preparation of CoMo HDS Catalysts Supported on Al2O3, TiO2 and ZrO2. *Catal. Today* **2008**, *130* (1), 41–49. https://doi.org/10.1016/J.CATTOD.2007.07.008.

(20) Bara, C.; Plais, L.; Larmier, K.; Devers, E.; Digne, M.; Lamic-Humblot, A.-F.; Pirngruber, G. D.; Carrier, X. Aqueous-Phase Preparation of Model HDS Catalysts on Planar Alumina Substrates: Support Effect on Mo Adsorption and Sulfidation. *J. Am. Chem. Soc.* **2015**, *137* (50), 15915–15928. https://doi.org/10.1021/jacs.5b10975.

(21) Jalilov, A. S.; Tanimu, A.; Ganiyu, S. A.; Alhooshani, K. Kinetic and Mechanistic Analysis of Dibenzothiophene Hydrodesulfurization on Ti-SBA-15–NiMo Catalysts. *Energy & Fuels* **2018**, *32* (11), 11383–11389. https://doi.org/10.1021/acs.energyfuels.8b02808.

(22) Copéret, C. *Catalysis by Transition Metal Sulphides. From Molecular Theory to Industrial Applications. H. Toulhoat and P. Raybaud, Editors, Technip Edition, Paris, 2013*; 2013; Vol. 307. https://doi.org/10.1016/j.jcat.2013.06.011.

(23) Song, C. An Overview of New Approaches to Deep Desulfurization for Ultra-Clean Gasoline, Diesel Fuel and Jet Fuel. *Catal. Today* **2003**, *86* (1), 211–263. https://doi.org/https://doi.org/10.1016/S0920-5861(03)00412-7.

(24) James G Speight. *The Desulfurization of Heavy Oils and Residua*, 2nd ed.; M.; MARCEL, DEKKER, INC, Eds.; Chemical industries, v. 78.: New York, NY, USA, 2000.

(25) Besenbacher, F.; Brorson, M.; Clausen, B. S.; Helveg, S.; Hinnemann, B.; Kibsgaard, J.; Lauritsen, J. V; Moses, P. G.; Nørskov, J. K.; Topsøe, H. Recent STM, DFT and HAADF-STEM Studies of Sulfide-Based Hydrotreating Catalysts: Insight into Mechanistic, Structural and Particle Size Effects. *Catal. Today* **2008**, *130* (1), 86–96. https://doi.org/10.1016/j.cattod.2007.08.009.

(26) Lauritsen, J. V; Kibsgaard, J.; Olesen, G. H.; Moses, P. G.; Hinnemann, B.; Helveg, S.; Nørskov,

1   J. K.; Clausen, B. S.; Topsøe, H.; Lægsgaard, E.; et al. Location and Coordination of Promoter

2   Atoms in Co- and Ni-Promoted MoS2-Based Hydrotreating Catalysts. *J. Catal.* **2007**, *249* (2), 220–

3   233. https://doi.org/10.1016/j.jcat.2007.04.013.

4   (27)   Krebs, E.; Daudin, A.; Raybaud, P. A DFT Study of CoMoS and NiMoS Catalysts: From Nano-

5   Crystallite Morphology to Selective Hydrodesulfurization. *Oil Gas Sci. Technol. - Rev. l'IFP* **2009**,

6   *64* (6), 707–718. https://doi.org/10.2516/ogst/2009004.

7   (28)   Lauritsen, J. V; Kibsgaard, J.; Helveg, S.; Topsøe, H.; Clausen, B. S.; Lægsgaard, E.; Besenbacher,

8   F. Size-Dependent Structure of MoS 2 Nanocrystals. *Nat. Nanotechnol.* **2007**, *2* (1), 53–58.

9   https://doi.org/10.1038/nnano.2006.171.

10   (29)   Grønborg, S. S.; Šarić, M.; Moses, P. G.; Rossmeisl, J.; Lauritsen, J. V. Atomic Scale Analysis of

11   Sterical Effects in the Adsorption of 4,6-Dimethyldibenzothiophene on a CoMoS Hydrotreating

12   Catalyst. *J. Catal.* **2016**, *344*, 121–128. https://doi.org/10.1016/j.jcat.2016.09.004.

13   (30)   Grush, M. M.; Christou, G.; Haemaelaeinen, K.; Cramer, S. P. Site-Selective XANES and EXAFS:

14   A Demonstration with Manganese Mixtures and Mixed-Valence Complexes. *J. Am. Chem. Soc.*

15   **1995**, *117* (21), 5895–5896. https://doi.org/10.1021/ja00126a047.

16   (31)   Glatzel, P.; Jacquamet, L.; Bergmann, U.; De Groot, F. M. F.; Cramer, S. P. Site-Selective EXAFS

17   in Mixed-Valence Compounds Using High-Resolution Fluorescence Detection: A Study of Iron in

18   Prussian Blue. *Inorg. Chem.* **2002**, *41* (12), 3121–3127. https://doi.org/10.1021/ic010709m.

19   (32)   Bordage, A.; Trannoy, V.; Proux, O.; Vitoux, H.; Moulin, R.; Bleuzen, A. In Situ Site-Selective

20   Transition Metal K-Edge XAS: A Powerful Probe of the Transformation of Mixed-Valence Com-

21   pounds.   *Phys.   Chem.   Chem.   Phys.*   **2015**,   *17*   (26),   17260–17265.

22   https://doi.org/10.1039/C5CP02591E.

(33) Glatzel, P.; Alonso-Mori, R.; Sokaras, D. Hard X-Ray Photon-in/Photon-out Spectroscopy: Instrumentation, Theory and Applications. In *X-Ray Absorption and X-Ray Emission Spectroscopy: Theory and Applications*; European Synchrotron Radiation Facility, Grenoble, France, 2015; Vol. 1–2, pp 125–153. https://doi.org/10.1002/9781118844243.ch6.

(34) Verbeni, R.; Kocsis, M.; Huotari, S.; Krisch, M.; Monaco, G.; Sette, F.; Vanko, G. Advances in Crystal Analyzers for Inelastic X-Ray Scattering. *J. Phys. Chem. Solids* **2005**, *66*, 2299–2305. https://doi.org/10.1016/j.jpcs.2005.09.079.

(35) Glatzel, P.; Sikora, M.; Smolentsev, G.; Fernández-García, M. Hard X-Ray Photon-in Photon-out Spectroscopy. *Catal. Today* **2009**, *145* (3–4), 294–299. https://doi.org/10.1016/j.cattod.2008.10.049.

(36) Visser, H.; Anxolabéhère-Mallart, E.; Bergmann, U.; Glatzel, P.; Robblee, J. H.; Cramer, S. P.; Girerd, J.-J.; Sauer, K.; Klein, M. P.; Yachandra, V. K. Mn K-Edge XANES and Kβ XES Studies of Two Mn - Oxo Binuclear Complexes: Investigation of Three Different Oxidation States Relevant to the Oxygen-Evolving Complex of Photosystem II. *J. Am. Chem. Soc.* **2001**, *123* (29), 7031–7039. https://doi.org/10.1021/ja004306h.

(37) Smolentsev, G.; Soldatov, A. V; Messinger, J.; Merz, K.; Weyhermüller, T.; Bergmann, U.; Pushkar, Y.; Yano, J.; Yachandra, V. K.; Glatzel, P. X-Ray Emission Spectroscopy to Study Ligand Valence Orbitals in Mn Coordination Complexes. *J. Am. Chem. Soc.* **2009**, *131* (36), 13161–13167. https://doi.org/10.1021/ja808526m.

(38) Glatzel, P.; Bergmann, U. High Resolution 1s Core Hole X-Ray Spectroscopy in 3d Transition Metal Complexes - Electronic and Structural Information. *Coord. Chem. Rev.* **2005**, *249* (1–2), 65–95. https://doi.org/10.1016/j.ccr.2004.04.011.

(39) Gandubert, A. D.; Legens, C.; Guillaume, D.; Rebours, S.; Payen, E. X-Ray Photoelectron Spectroscopy Surface Quantification of Sulfided CoMoP Catalysts - Relation between Activity and Promoted Sites Part I: Influence of the Co/Mo Ratio. *Oil Gas Sci. Technol.* **2007**, *62* (1), 79–89. https://doi.org/10.2516/ogst:2007007.

(40) Gandubert, A. D.; Legens, C.; Guillaume, D.; Payen, E. X-Ray Photoelectron Spectroscopy Surface Quantification of Sulfided CoMoP Catalysts. Relation between Activity and Promoted Sites. Part II: Influence of the Sulfidation Temperature. *Surf. Interface Anal.* **2006**, *38* (4), 206–209. https://doi.org/10.1002/sia.2249.

(41) Frizi, N.; Blanchard, P.; Payen, E.; Baranek, P.; Rebeilleau, M.; Dupuy, C.; Dath, J. P. Genesis of New HDS Catalysts through a Careful Control of the Sulfidation of Both Co and Mo Atoms: Study of Their Activation under Gas Phase. *Catal. Today* **2008**, *130* (2–4), 272–282. https://doi.org/10.1016/j.cattod.2007.10.109.

(42) Ninh, T. K. T.; Laurenti, D.; Leclerc, E.; Vrinat, M. Support Effect for CoMoS and CoNiMoS Hydrodesulfurization Catalysts Prepared by Controlled Method. *Appl. Catal. A Gen.* **2014**, *487*, 210–218. https://doi.org/https://doi.org/10.1016/j.apcata.2014.07.042.

(43) Rochet, A.; Baubet, B.; Moizan, V.; Devers, E.; Hugon, A.; Pichon, C.; Payen, E.; Briois, V. Influence of the Preparation Conditions of Oxidic NiMo/Al$_2$O$_3$ Catalysts on the Sulfidation Ability: A Quick-XAS and Raman Spectroscopic Study. *J. Phys. Chem. C* **2015**, *119* (42), 23928–23942. https://doi.org/10.1021/acs.jpcc.5b06219.

(44) Rochet, A.; Ribeiro Passos, A.; Legens, C.; Briois, V. Sulphidation Study of a Dried Ni/Al2O3 Catalyst by Time-Resolved XAS-MS Combined with in Situ Raman Spectroscopy and Multivariate Quick-XAS Data Analysis. *Catal. Struct. React.* **2017**, *3* (1–2), 33–42. https://doi.org/10.1080/2055074X.2016.1263178.

(45) Lesage, C.; Devers, E.; Legens, C.; Fernandes, G.; Roudenko, O.; Briois, V. High Pressure Cell for Edge Jumping X-Ray Absorption Spectroscopy: Applications to Industrial Liquid Sulfidation of Hydrotreatment Catalysts. *Catal. Today* **2019**, *336*, 63–73. https://doi.org/10.1016/j.cattod.2019.01.081.

(46) Gaur, A.; Hartmann Dabros, T. M.; Høj, M.; Boubnov, A.; Prüssmann, T.; Jelic, J.; Studt, F.; Jensen, A. D.; Grunwaldt, J.-D. Probing the Active Sites of MoS $_2$ Based Hydrotreating Catalysts Using Modulation Excitation Spectroscopy. *ACS Catal.* **2019**, *9* (3), 2568–2579. https://doi.org/10.1021/acscatal.8b04778.

(47) van Haandel, L.; Longo, A.; Bras, W.; Hensen, E. J. M.; Weber, T. Activation of Co−Mo−S Hydrodesulfurization Catalysts Under Refinery Conditions-A Combined SAXS/XAS Study. *ChemCatChem* **2019**, *11* (20), 5013–5017. https://doi.org/10.1002/cctc.201901390.

(48) Papadopoulou, C.; Vakros, J.; Matralis, H. K.; Voyiatzis, G. A.; Kordulis, C. Preparation, Characterization, and Catalytic Activity of CoMo/Gamma-Al2O3 Catalysts Prepared by Equilibrium Deposition Filtration and Conventional Impregnation Techniques. *J. Colloid Interface Sci.* **2004**, *274* (1), 159–166. https://doi.org/10.1016/j.jcis.2003.11.041.

(49) Rueff, J.-P.; Ablett, J. M.; Ceolin, D.; Prieur, D.; Moreno, T.; Baledent, V.; Lassalle-Kaiser, B.; Rault, J. E.; Simon, M.; Shukla, A. The GALAXIES Beamline at the SOLEIL Synchrotron: Inelastic X-Ray Scattering and Photoelectron Spectroscopy in the Hard X-Ray Range. *J. Synchrotron Radiat.* **2015**, *22* (1), 175–179.

(50) La Fontaine, C.; Barthe, L.; Rochet, A.; Briois, V. X-Ray Absorption Spectroscopy and Heterogeneous Catalysis: Performances at the SOLEIL's SAMBA Beamline. *Catal. Today* **2013**, *205*, 148–158. https://doi.org/https://doi.org/10.1016/j.cattod.2012.09.032.

(51) N. Fairley. CasaXPS.

(52) Grosvenor, A. P.; Wik, S. D.; Cavell, R. G.; Mar, A. Examination of the Bonding in Binary Transition-Metal Monophosphides MP (M = Cr, Mn, Fe, Co) by X-Ray Photoelectron Spectroscopy. *Inorg. Chem.* **2005**, *44* (24), 8988–8998. https://doi.org/10.1021/ic051004d.

(53) Biesinger, M. C.; Payne, B. P.; Grosvenor, A. P.; Lau, L. W. M.; Gerson, A. R.; Smart, R. S. C. Resolving Surface Chemical States in XPS Analysis of First Row Transition Metals, Oxides and Hydroxides: Cr, Mn, Fe, Co and Ni. *Appl. Surf. Sci.* **2011**, *257* (7), 2717–2730. https://doi.org/https://doi.org/10.1016/j.apsusc.2010.10.051.

(54) Joly, Y. X-Ray Absorption near-Edge Structure Calculations beyond the Muffin-Tin Approximation. *Phys. Rev. B* **2001**, *63* (12), 125120. https://doi.org/10.1103/PhysRevB.63.125120.

(55) Krause, M. O.; Oliver, J. H. Natural Widths of Atomic K and L Levels, Kα X-ray Lines and Several KLL Auger Lines. *J. Phys. Chem. Ref. Data* **1979**, *8* (2), 329–338. https://doi.org/10.1063/1.555595.

(56) Perdew, J. P.; Burke, K.; Ernzerhof, M. Generalized Gradient Approximation Made Simple. *Phys. Rev. Lett.* **1996**, *77* (18), 3865–3868. https://doi.org/10.1103/PhysRevLett.77.3865.

(57) Kresse, G.; Hafner, J. Ab Initio Molecular Dynamics for Open-Shell Transition Metals. *Phys. Rev. B* **1993**, *48* (17), 13115–13118. https://doi.org/10.1103/PhysRevB.48.13115.

(58) Kresse, G.; Furthmüller, J. Efficient Iterative Schemes for Ab Initio Total-Energy Calculations Using a Plane-Wave Basis Set. *Phys. Rev. B* **1996**, *54* (16), 11169–11186. https://doi.org/10.1103/PhysRevB.54.11169.

(59) Http://cms.mpi.univie.ac.at/vasp., V. 4. 6. A. at. No Title.

(60) Kresse, G.; Joubert, D. From Ultrasoft Pseudopotentials to the Projector Augmented-Wave Method. *Phys. Rev. B* **1999**, *59* (3), 1758–1775. https://doi.org/10.1103/PhysRevB.59.1758.

1 (61) Blöchl, P. E. Projector Augmented-Wave Method. *Phys. Rev. B* **1994**, *50* (24), 17953–17979.

2 https://doi.org/10.1103/PhysRevB.50.17953.

3 (62) Kurian, R.; van Schooneveld, M. M.; Zoltán, N.; Vankó, G.; de Groot, F. M. F. Temperature-De-

4 pendent 1s2p Resonant Inelastic X-Ray Scattering of CoO. *J. Phys. Chem. C* **2013**, *117* (6), 2976–

5 2981. https://doi.org/10.1021/jp3101859.

6 (63) Groot, F. de. Multiplet Effects in X-Ray Spectroscopy. *Coord. Chem. Rev.* **2005**, *249* (1), 31–63.

7 https://doi.org/https://doi.org/10.1016/j.ccr.2004.03.018.

8 (64) Thole, B. T.; Van Der Laan, G.; Butler, P. H. Spin-Mixed Ground State of Fe Phthalocyanine and

9 the Temperature-Dependent Branching Ratio in X-Ray Absorption Spectroscopy. *Chem. Phys.*

10 *Lett.* **1988**, *149*, 295–299. https://doi.org/10.1016/0009-2614(88)85029-2.

11 (65) Thole, B. T.; van der Laan, G.; Fuggle, J. C.; Sawatzky, G. A.; Karnatak, R. C.; Esteva, J.-M. 3d

12 X-Ray-Absorption Lines and the 3d94fn+1multiplets of the Lanthanides. *Phys. Rev. B* **1985**, *32*

13 (8), 5107–5118. https://doi.org/10.1103/PhysRevB.32.5107.

14 (66) Kramers, H. A.; Heisenberg, W. Über Die Streuung von Strahlung Durch Atome. *Zeitschrift für*

15 *Phys.* **1925**, *31* (1), 681–708. https://doi.org/10.1007/BF02980624.

16 (67) Gel'mukhanov, F.; Ågren, H. Resonant X-Ray Raman Scattering. *Phys. Rep.* **1999**, *312* (3), 87–

17 330. https://doi.org/https://doi.org/10.1016/S0370-1573(99)00003-4.

18 (68) Stavitski, E.; de Groot, F. M. F. The CTM4XAS Program for EELS and XAS Spectral Shape Anal-

19 ysis of Transition Metal L Edges. *Micron* **2010**, *41* (7), 687–694.

20 https://doi.org/https://doi.org/10.1016/j.micron.2010.06.005.

21 (69) Bagger, A.; Haarman, T.; Puig Molina, A.; Moses, P. G.; Ishii, H.; Hiraoka, N.; Wu, Y.-H.; Tsuei,

22 K.-D.; Chorkendorff, I.; De Groot, F. 1s2p Resonant Inelastic X-Ray Scattering Combined Dipole

and Quadrupole Analysis Method. *J. Synchrotron Radiat.* **2017**, *24* (1), 296–301.

(70) Jiménez-Mier, J.; van Ek, J.; Ederer, D. L.; Callcott, T. A.; Jia, J. J.; Carlisle, J.; Terminello, L.; Asfaw, A.; Perera, R. C. Dynamical Behavior of X-Ray Absorption and Scattering at the L Edge of Titanium Compounds: Experiment and Theory. *Phys. Rev. B* **1999**, *59* (4), 2649–2658. https://doi.org/10.1103/PhysRevB.59.2649.

(71) Rubensson, J.-E. BEISIN. *J. Electron Spectros. Relat. Phenomena* **2000**, *110–111*, 135–151. https://doi.org/https://doi.org/10.1016/S0368-2048(00)00161-4.

(72) Gandubert, A. D.; Krebs, E.; Legens, C.; Costa, D.; Guillaume, D.; Raybaud, P. Optimal Promoter Edge Decoration of CoMoS Catalysts: A Combined Theoretical and Experimental Study. *Catal. Today* **2008**, *130* (1), 149–159. https://doi.org/10.1016/j.cattod.2007.06.041.

(73) Raybaud, P.; Hafner, J.; Kresse, G.; Toulhoat, H. Ab Initiodensity Functional Studies of Transition-Metal Sulphides: II. Electronic Structure. *J. Phys. Condens. Matter* **1997**, *9* (50), 11107–11140. https://doi.org/10.1088/0953-8984/9/50/014.

(74) Castner, D. G.; Watson, P. R. X-Ray Absorption Spectroscopy and x-Ray Photoelectron Spectroscopy Studies of Cobalt Catalysts. 3. Sulfidation Properties in Hydrogen Sulfide/Hydrogen. *J. Phys. Chem.* **1991**, *95* (17), 6617–6623. https://doi.org/10.1021/j100170a044.

(75) Townsend, M. G.; Horwood, J. L.; Tremblay, R. J.; Ripley, L. G. On the Metallic Character of Co9S8 and (Fe, Ni)9S8. *Phys. status solidi* **1972**, *9* (2), K137–K139. https://doi.org/10.1002/pssa.2210090252.

(76) Topsøe, H.; Clausen, B. S.; Candia, R.; Wivel, C.; Mørup, S. In Situ Mössbauer Emission Spectroscopy Studies of Unsupported and Supported Sulfided Co☐Mo Hydrodesulfurization Catalysts: Evidence for and Nature of a Co☐Mo☐S Phase. *J. Catal.* **1981**, *68* (2), 433–452. https://doi.org/https://doi.org/10.1016/0021-9517(81)90114-7.

1 (77) Castle, J. E. *Practical Surface Analysis by Auger and X-Ray Photoelectron Spectroscopy. D. Briggs*

2   *and M. P. Seah (Editors). John Wiley and Sons Ltd, Chichester, 1983, 533 Pp., £44.50*; John Wiley

3   & Sons, Ltd, 1984; Vol. 6. https://doi.org/10.1002/sia.740060611.

4 (78) Guda, A. A.; Smolentsev, N.; Rovezzi, M.; Kaidashev, E. M.; Kaydashev, V. E.; Kravtsova, A. N.;

5   Mazalova, V. L.; Chaynikov, A. P.; Weschke, E.; Glatzel, P.; et al. Spin-Polarized Electronic Struc-

6   ture of the Core-Shell ZnO/ZnO:Mn Nanowires Probed by X-Ray Absorption and Emission Spec-

7   troscopy. *J. Anal. At. Spectrom.* **2013**, *28* (10), 1629–1637. https://doi.org/10.1039/c3ja50153a.

8 (79) Kühn, T.-J.; Caliebe, W.; Matoussevitch, N.; Bönnemann, H.; Hormes, J. Site-Selective X-Ray

9   Absorption Spectroscopy of Cobalt Nanoparticles. *Appl. Organomet. Chem.* **2011**, *25* (8), 577–

10   584. https://doi.org/10.1002/aoc.1805.

11 (80) Wang, X.; de Groot, F. M. F.; Cramer, S. P. Spin-Polarized x-Ray Emission of 3d Transition-Metal

12   Ions: A Comparison via Kα and Kβ Detection. *Phys. Rev. B* **1997**, *56* (8), 4553–4564.

13   https://doi.org/10.1103/PhysRevB.56.4553.

14 (81) Topsøe, H. The Role of Co–Mo–S Type Structures in Hydrotreating Catalysts. *Appl. Catal. A Gen.*

15   **2007**, *322*, 3–8. https://doi.org/https://doi.org/10.1016/j.apcata.2007.01.002.

16

1

2

1